Balloon-borne measurements of temperature, water vapor, ozone and aerosol backscatter at the southern slopes of the Himalayas during StratoClim 2016-2017

Simone Brunamonti[1], Teresa Jorge[1], Peter Oelsner[2], Sreeharsha Hanumanthu[3,4], Bhupendra B. Singh[3], K. Ravi Kumar[3,10], Sunil Sonbawne[3], Susanne Meier[2], Deepak Singh[5], Frank G. Wienhold[1], Bei Ping Luo[1], Maxi Boettcher[1], Yann Poltera[1], Hannu Jauhiainen[8], Rijan Kayastha[6], Jagadishwor Karmacharya[9], Ruud Dirksen[2], Manish Naja[5], Markus Rex[7], Suvarna Fadnavis[3] and Thomas Peter[1]

[1]Institute for Atmospheric and Climate Science (IAC), Swiss Federal Institute of Technology (ETH), Zürich, Switzerland
[2]Deutscher Wetterdienst (DWD) / GCOS Reference Upper Air Network (GRUAN) Lead Center, Lindenberg, Germany
[3]Indian Institute of Tropical Meteorology (IITM), Pune, India
[4]Forschungszentrum Jülich (FZJ), Institute of the Energy and Climate Research – Stratosphere (IEK-7), Jülich, Germany
[5]Aryabhatta Research Institute of Observational Sciences (ARIES), Nainital, India
[6]Kathmandu University (KU), Dhulikhel, Nepal
[7]Alfred Wegener Institute (AWI) for Polar and Marine Research, Potsdam, Germany
[8]Vaisala Oyj, Vantaa, Finland
[9]Department of Hydrology and Meteorology (DHM), Meteorological Forecasting Division, Kathmandu, Nepal
[10]*Now at* Centre for Atmospheric Sciences, Indian Institute of Technology (IIT), Delhi, India

Correspondence to: Simone Brunamonti (simone.brunamonti@env.ethz.ch)

Abstract. The Asian summer monsoon anticyclone (ASMA) is a major meteorological system of the upper troposphere-lower stratosphere (UTLS) during boreal summer. It is known to contain enhanced tropospheric trace gases and aerosols, due to rapid lifting from the boundary layer by deep convection and subsequent horizontal confinement. Given its dynamical structure, the ASMA represents an efficient pathway for the transport of pollutants to the global stratosphere. Detailed understanding of the thermal structure and processes in ASMA requires accurate in-situ measurements. Within the StratoClim project we performed state-of-the-art balloon-borne measurements of temperature, water vapor, ozone and aerosol backscatter from two stations at the southern slopes of the Himalayas. In total, 63 balloon soundings were conducted during two extensive monsoon-season campaigns, in August 2016 in Nainital, India (29.4°N, 79.5°E) and in July-August 2017 in Dhulikhel, Nepal (27.6°N, 85.5°E), and one shorter post-monsoon campaign in November 2016 in Nainital. These measurements provide unprecedented insights into the UTLS thermal structure, the vertical distributions of water vapor, ozone and aerosols, cirrus cloud properties and interannual variability in ASMA. Here we provide an overview of all the data collected during the three campaign periods, with focus on the UTLS region and the monsoon season. We analyze the vertical structure of ASMA in terms of significant levels and layers, identified from the temperature and potential temperature lapse rates and Lagrangian backward trajectories, providing a framework for relating the measurements to local thermodynamic properties and the large-scale anticyclonic flow. Both the monsoon-season campaigns show evidence of deep convection and confinement extending up to 1.5-2 km above the

cold-point tropopause (CPT), yielding a body of air with high water vapor and low ozone which is prone to be lifted further and mixed into the free stratosphere. Enhanced aerosol backscatter also reveals the signature of the Asian tropopause aerosol layer (ATAL) over the same region of altitudes. The Dhulikhel 2017 campaign was characterized by an on average 5 K colder CPT than in Nainital 2016 and a local water vapor maximum in the confined lower stratosphere, about 1 km above the CPT. Data assessment and modeling studies are currently ongoing with the aim to fully explore this dataset and its implications with respect to stratospheric moistening via the ASMA system and related processes.

1. Introduction

Large-scale deep convection associated with the Asian summer monsoon (ASM) during boreal summer induces a strong and persistent anticyclonic vortex in the upper troposphere-lower stratosphere (UTLS), known as ASM anticyclone (ASMA) (e.g. Hoskins and Rodwell, 1995) or, previously, as Tibetan high (e.g. Krishnamurti and Bhalme, 1976). The ASMA is confined by the subtropical westerly jet stream to the north (40-45°N) and the equatorial easterly jet stream to the south (10-15°N), and spans roughly one third of the northern hemisphere's longitudes (20-140°E). Its geographic center is above the Tibetan plateau and the altitude of maximum strength of the anticyclonic circulation is around the local tropopause (17-18 km), which is the highest worldwide during the ASM season (e.g. Dethof et al., 1999; Bian et al., 2012; Garny and Randel, 2016; Ploeger et al., 2015; Pan et al., 2016). The ASMA is subject to strong dynamical variability, oscillations and eddy shedding (e.g. Randel and Park, 2006; Yan et al., 2012; Garny and Randel, 2013; Vogel et al., 2014; Nützel et al., 2016).

From satellite measurements, the ASMA is known to be enriched in tropospheric trace species and pollutants, including water vapor, carbon monoxide, methane, hydrogen cyanide, peroxyacetil nitrate (Randel et al., 2001; 2010; Park et al., 2004; 2007; 2008; Fadnavis et al., 2014; Ungermann et al., 2016), and aerosols, forming the Asian tropopause aerosol layer (ATAL) (Vernier et al., 2011; 2015; Thomason and Vernier, 2013). This is due to persistent deep convection over heavily polluted regions, such as the Indian subcontinent and south-east Asia, lifting pollutants from the boundary layer to the upper troposphere, where the anticyclonic winds keep the air masses horizontally confined. The unique dynamical structure of the ASMA, with tropopause located at higher potential temperature than all its surroundings (θ > 380 K), provides a potentially very efficient pathway for the transport of these pollutants into the lower stratosphere. Transport across the tropopause can occur either vertically above the ASMA, by radiative-driven slow ascent (e.g. Garny and Randel, 2016) or overshooting convection (Fu et al., 2006) ("chimney model"), or adiabatically across the horizontal boundaries of ASMA, hence bypassing the cold-point tropopause ("blower model") (Pan et al., 2016). Lagrangian trajectory calculations suggest that about half of the air mass in ASMA enters the stratosphere by the end of the ASM season (Garny and Randel, 2016), yet which transport pathway is the most effective is currently debated (e.g. Orbe et al., 2015; Garny and Randel, 2016; Pan et al., 2016; Ploeger et al., 2017).

Lagrangian trajectories were also used to investigate the origin of the air masses in ASMA (Bergman et al., 2013; Vogel et al., 2015), although this approach is limited by the convective nature of the transport. Nevertheless, these studies are consistent with satellite observations (Fu et al., 2006), regional weather forecasting (Heath and Fuelberg, 2014) and global atmospheric circulation models (Fadnavis et al., 2013; Pan et al., 2016) in indicating the region of the southern slopes of the Himalayas (i.e. latitudes 25-35°N south of the Tibetan plateau, approximately) as a hot-spot for the transport of boundary layer pollutants to ASMA. Considering the recent rapid increase of pollutant emissions from India (Krotkov et al., 2016), it is crucial for global chemistry climate models to properly represent the ASMA dynamics, thermodynamic structure and processes.

Up to date, most of the observational evidence regarding the chemical composition of the Asian UTLS is derived from satellite measurements, providing information with good regional and temporal coverage, but with limited vertical resolution. Highly vertically-resolved datasets in the UTLS are important to understand the physical boundaries that control the vertical distribution of chemical species, and microphysical processes like the nucleation of cirrus clouds and aerosols. This requires accurate in-situ measurements in ASMA. Aircraft measurements are available from dedicated campaigns (e.g. Gottschaldt et al., 2018) or civil aviation-based observational networks (e.g. Rauthe-Schöch et al., 2016), yet these are either sparse in space and time, or limited by the relatively low cruising altitude of passenger aircrafts (10-12 km). Balloon-borne measurements are particularly suited for the investigation of the UTLS, and balloon campaigns dedicated to the study of the ASMA and ATAL increased in frequency over the last decade (e.g. Bian et al., 2012; Vernier et al., 2018; this work).

In this article we present and discuss the data collected by the StratoClim balloon campaigns, carried out from two sites at the southern slopes of the Himalayas through the years 2016 and 2017. State-of-the-art instruments were used to measure vertical profiles of temperature, water vapor, ozone and aerosol backscatter, from the surface to the middle stratosphere. Here we first provide an overview of all measurements, showing mean profiles and their standard deviation ranges of natural variability for the different campaign periods, and then focus on analyzing the thermodynamic structure of the UTLS during the ASM season and how it relates with the vertical distributions of water vapor, ozone and aerosols. One aim of this work is also to pave the way for ongoing more targeted modeling and intercomparison studies within StratoClim and other activities.

2. Campaign description, instruments and data processing

The measurements were performed in Nainital, Uttarakhand, India (29.35°N, 79.46°E: NT) and Dhulikhel, Nepal (27.62°N, 85.54°E: DK), hosted respectively by the Aryabhatta Research Institute of Observational Sciences (ARIES) and Kathmandu University (KU). Both sites are located at the southern slopes of the Himalayan mountain range, at elevations of 1820 m (NT) and 1530 m (DK) above sea level. In this region, the terrain elevation increases steeply from sea-level heights of the Indo-Gangetic plane to the south, to elevations above 3000 m of the Tibetan plateau to the north. Strong orographic forcing induces persistent deep convection and heavy rainfall during the monsoon season (Vellore et al., 2016).

The measurements were conducted during three distinct periods of time, including two extensive monsoon-season campaigns, in NT in 2016 (2-31 August, 30 balloon soundings: $NT16_{AUG}$) and in DK in 2017 (30 July - 12 August, 28 balloon soundings: DK17), and one shorter post-monsoon campaign in NT (2-8 November 2016, 5 balloon soundings: $NT16_{NOV}$) (note that a list of the main acronyms used in this paper, including the abbreviations of stations and campaign periods, is given in Table 1). The frequency of the soundings and the composition of the payloads varied depending on meteorological conditions and on operational constraints. Various logistic limitations affected our DK17 campaign, resulting in a reduced measurement schedule (most notably, the number of backscatter measurements was limited). Nevertheless, important scientific data were collected. The DK17 campaign took place simultaneously with the StratoClim aircraft campaign, based in Kathmandu Airport (Nepal), which performed 8 scientific flights with the high-altitude Geophysica-M55 research aircraft.

All soundings employed meteorological latex balloons (Totex, Japan) filled with hydrogen gas in order to ascend at a rate of about 5 m/s. Maximum burst altitude of these balloons is around 35 km, and more than 70% of our soundings reached at least 30 km (see Table S1 in supplementary material). A standard meteorological radiosonde was used to host additional instruments through its XDATA interface (Oelsner and Tietz, 2017), and to transmit the data of all instruments to the ground station at 1 Hz frequency. In particular, we used RS41-SGP (Vaisala, Finland) radiosondes (Vaisala, 2017), and the DigiCora MW41 sounding system (Vaisala, Finland) as ground station (Vaisala, 2014). Additional instruments employed were: Electrochemical Concentration Cell (ECC, manufacturer: En-Sci, USA) (Komhyr, 1969) for ozone (O_3) mixing ratio, Cryogenic Frost-point Hygrometer (CFH, En-Sci, USA) (Vömel et al., 2007; 2016) for water vapor (H_2O) mixing ratio, and the Compact Optical Backscatter Aerosol Detector (COBALD, MyLab, Switzerland) for aerosol backscatter.

For the pressure (p) and temperature (T) measurements that we analyze in this work, uncertainties of RS41-SGP (hereafter: RS41) given by the manufacturer are 0.6/1 hPa (at pressures lower/higher than 100 hPa) and 0.3/0.4 K (at altitudes lower/higher than 16 km), respectively. The performances of ECC sondes have been assessed by many studies (e.g. Smit et al., 2007), and uncertainties are estimated as 5-10% in terms of O_3 partial pressure. CFH is a frost-point hygrometer based on the chilled-mirror principle with uncertainty on H_2O mixing ratio lower than 10% up to 28 km altitude (Vömel et al., 2007). ECC and CFH are regularly deployed in the ASM region since 2009 (Bian et al., 2012). COBALD is a detector for aerosol backscatter measurements at optical wavelengths of 455 nm (blue visible) and 940 nm (infrared) developed at ETH Zürich, downscaling the original backscatter sonde by Rosen and Kjome (1991) in weight and size. COBALD is able to detect cirrus clouds (e.g. Brabec et al., 2012) as well as aerosol layers, such as ATAL (Vernier et al., 2015). In addition, one RS92-SGP radiosonde (Vaisala, Finland) was added to almost all payloads for an intercomparison with the performances of RS41 (not discussed in this paper). Finally, we note that for logistical constraints, the first two soundings in $NT16_{AUG}$ employed iMet-1-RSB radiosondes (InterMet, USA) (InterMet, 2006), offering the XDATA interface (Wendell and Jordan, 2016), instead of RS41, and SkySonde version 1.9 (Jordan and Hall, 2016) as data acquisition software.

In this study, we use the pressure measured by RS41 as the main vertical coordinate for all instruments. All variables are binned in pressure intervals of 1 hPa for $p > 300$ hPa, and 0.5 hPa for $p < 300$ hPa, yielding an improved signal-to-noise ratio and a dataset with consistent vertical levels. This binning corresponds to a vertical resolution of approximately 25 m in the UTLS. A quality check is performed for all instruments, based on interpretation of their house-keeping data, and data points showing anomalous behavior are rejected. In this context, the contamination of CFH measurements deserves a special mention, as this effect was observed in a significant number of cases. It consists in the drift towards high frost-point temperatures in the stratosphere, corresponding to water vapor mixing ratios exceeding physical constraints (see Figure S1 in supplementary material), which we attribute to the deposition of supercooled water droplets onto the inner walls of the instrument's inlet tube

while passing through mixed-phase clouds. This hypothesis is currently subject of a dedicated modeling study. To avoid such instrumental artifact, for the analysis in this paper we do not accept H_2O mixing ratio measurements higher than 10 ppmv in the stratosphere, which are unrealistic, as well as all measurements at pressures below 20 hPa (see Section 3). Ice saturation (S_{ice}), i.e. relative humidity with respect to ice, is calculated using the frost-point temperature measured by CFH, air temperature by RS41, and the parameterization for saturation vapor pressure over ice by Murphy and Koop (2005). The COBALD data are expressed as backscatter ratio (BSR), i.e. the ratio of the total-to-molecular backscatter coefficient. This is calculated by dividing the total measured signal to its molecular contribution, which is computed from the atmospheric extinction according to Bucholtz (1995), and using air density derived from the measurements of temperature and pressure (Cirisian et al., 2014). Uncertainty on COBALD BSR as inferred by this technique is estimated around 5% (Vernier et al., 2015).
The number of deployments of each instrument during the different campaign periods are summarized in Table 2. A full list of all 63 balloon soundings with date and time of launch, payload description, burst altitude and notes on malfunctionings and contamination events is given in Table S1 in supplementary material. Note that, for conversion of pressure to geometric altitude (z), mean profiles of p vs. z measured by RS41 are also shown in Figure S2 in supplementary material.

3. Data overview

Figure 1 shows mean profiles and standard deviations of temperature, H_2O mixing ratio and O_3 mixing ratio calculated from all measurements performed during the three campaign periods, namely $NT16_{AUG}$ (blue), $NT16_{NOV}$ (green) and DK17 (red). Panels a-c show the entire measured profiles, while panels d-f show zooms into the UTLS region. In this section we briefly discuss their main features. Aerosol backscatter measurements will be discussed in Section 6.
In the troposphere, average H_2O mixing ratios differ by up to a factor of 40 between the dry (November) and the ASM season (July-August). Massive latent heat release by condensation during the wet period, in contrast to dry conditions in winter, is reflected in different lower tropospheric lapse rates for the two seasons, with about 5.5 K/km in July-August, and 8 K/km in November. This is consistent with the meridional shift of the intertropical convergence zone (ITCZ) and the associated deep convection patterns in the Asian sector, reaching about 30°N in boreal summer (Lawrence and Lelieveld, 2010). Lower tropospheric O_3 in $NT16_{AUG}$ compared to $NT16_{NOV}$ is likely due to enhanced washout of ozone precursor gases during the monsoon season. Higher tropospheric O_3 in $NT16_{AUG}$ vs. DK17 might be related to photochemical smog transport from the New Delhi urban area and the highly populated Indo-Gangetic plane (e.g. Kumar et al., 2010).
The structure of the tropopause region is very different during the three measurement periods. In contrast to the sharp cold-point tropopause (CPT) of the ASM season, the November measurements show an almost isothermal layer above the lapse-rate tropopause (LRT, defined according to the World Meteorological Organization: WMO, 1957), such that in $NT16_{AUG}$ and DK17 the LRT coincides with the CPT, while in $NT16_{NOV}$ the average LRT and CPT are about 2.5 km apart. Seasonal variations of the LRT-CPT separation are consistent with Munchak and Pan (2014) and related to varying meridional position of the jet stream (see Section 4.1). Interestingly, comparing the two ASM season datasets also reveals significant differences. The

average CPT is 10 hPa higher (88 vs. 97.5 hPa), corresponding to about 600 m in altitude, and 5 K colder (-81.7 vs. -76.8 °C) in DK17 compared to $NT16_{AUG}$. Water vapor in the UTLS is minimum in $NT16_{NOV}$, with mixing ratios around 2.5 ppmv above the LRT. During the ASM, UTLS H_2O is higher, but different vertical distributions are observed. In $NT16_{AUG}$, H_2O mixing ratio decreases monotonically with altitude, with mean value of 6.8 ppmv at the CPT. In DK17, H_2O mixing ratio shows a minimum at the CPT (3.5 ppmv), and a local maximum above it (6 ppmv). Mean altitude, pressure, potential temperature and temperature of the LRT and CPT for the three campaign periods are summarized in Table 3.

Lower stratospheric temperatures (20-60 hPa) differ by about 2-4 K between November and July-August, which is consistent with the climatological annual cycle of stratospheric temperature (Randel et al., 2003). Stratospheric H_2O mixing ratios are in the range of 4-6 ppmv up to 20 hPa, with a slight increase with altitude due to oxidation of methane. Above approximately 20 hPa (27 km), all CFH measurements show an unrealistic increase in H_2O mixing ratio, which is a measurement artifact. At such high altitudes and low air densities, outgassing from the balloon skin and the payload train can play a significant role in contaminating the humidity measurements (Kräuchi et al., 2016). Water vapor data in this range will not be considered in this analysis. Differences in stratospheric ozone between $NT16_{AUG}$ and DK17 are likely due to interannual variability.

4. Meteorological overview

For relating the measurements to the large-scale atmospheric flow, here we analyze meteorological data from the European Center for Medium-range Weather Forecast (ECMWF) for the three campaign periods.

4.1 Seasonal variability

Figure 2 illustrates the seasonal variability of the meteorological systems above the southern slopes of the Himalayas during $NT16_{AUG}$ (top row), $NT16_{NOV}$ (center), and DK17 (bottom row). The left column (panels a, c, e) shows latitude-pressure cross sections of potential vorticity (PV), potential temperature and total wind speed for NT (longitude 80°E, panels a, c) and DK (85°E, panel e), from ECMWF analysis data averaged over the time of the respective measurement periods. The right column (panels d, b, f) shows average geopotential height at 100 hPa for the three measurement periods from ECMWF analysis data, superimposed with 2-weeks backward air mass trajectories initialized at 100 hPa at the time of each sounding during the three campaign periods. Trajectories are calculated by the Lagrangian Analysis Tool (LAGRANTO) (Wernli and Davies, 1997) using ERA-Interim re-analysis wind fields and color-coded with pressure.

During the $NT16_{AUG}$ and DK17 campaigns (panels a-b, e-f), our stations are located inside the ASMA vortex. The continental-scale anticyclonic motion is confined by the subtropical westerly jet stream to the north (40-45°N), and the equatorial easterly jet to the south (10-15°N). Both NT and DK, during their respective measurement periods, are found in the region of average geopotential height exceeding 16.8 km at 100 hPa, which is the highest in ASMA. Backward trajectories show that the UTLS flow at the southern slopes of the Himalayas is mainly easterly, following the southern branch of the ASMA, and transporting air masses which were confined inside the anticyclone already for several days. During the last 2 weeks prior to their respective measurement, the air masses sampled at 100 hPa during our campaigns undergo net diabatic ascent, at an average rate of 0.7 K/day and 0.4 K/day (in isentropic coordinates) for $NT16_{AUG}$ and DK17, respectively. The equatorial easterly jet was slightly stronger and extended further north during the ASM season 2017 (panel e) compared to 2016 (a) which is also reflected by the corresponding backward trajectories (b, f). North of the subtropical westerly jet, the dynamical tropopause (corresponding to PV = 3-4 PVU in this region and season: Kunz et al., 2011) decreases steeply with altitude.

After the end of the monsoon season, the subtropical westerly jet migrates southward to 30-35°N and intensifies in strength. Therefore, during the post-monsoon campaign $NT16_{NOV}$ (panels c-d), our station is located below the jet stream and the associated tropopause break, resulting in the large LRT-CPT separation discussed in Section 3. In contrast to the ASM season, in November the UTLS winds at the southern slopes of the Himalayas are mainly westerly and follow the subtropical jet stream. This is consistent with wind speed and wind direction measurements by RS41 shown in Figure S3 in supplementary material. We also note that the large standard deviation of UTLS temperature in $NT16_{NOV}$ (Figure 1d) is likely related to varying meridional position of the jet stream during the measurement period.

The dynamical features discussed above are consistent with the seasonal variations of the ITCZ, the jet streams and the ASM system in general, which are extensively discussed in previous literature, e.g. Lawrence and Lieleveld (2010), Munchak and Pan (2014), Ploeger et al. (2015), Garny and Randel (2016), Pan et al. (2016).

4.2 Interannual and regional variability

To assess whether the differences between the observations in $NT16_{AUG}$ and DK17 are caused mainly by geographic difference, and associated different mesoscale weather features, or by interannual variability between the ASM 2016 and 2017 seasons, Figure 3 shows time series of UTLS temperature (left column) and H_2O mixing ratio (right column) from ECMWF analysis data for both stations and both campaign periods.

In August 2016 (panels a-d) the UTLS was relatively warm at both locations, with CPT temperatures rarely below -80°C and DK slightly colder than NT (0.4 K on average at 100 hPa), and H_2O mixing ratio did never decrease below 4.5 ppmv at both sites. The same day-to-day variability features occur at both locations with a time shift of about 6-12 h, which is consistent with DK being systematically upstream of NT along the southern branch of the ASMA, and a wind speed of around 20 m/s in the UTLS. In July-August 2017 (panels e-h), temperatures and H_2O values and features are similar to 2016 until 3 August. Then, a period characterized by extremely cold and dry tropopause starts in both NT and DK, peaking between 7-10 August with CPT colder than -83°C and H_2O mixing ratios lower than 3 ppmv. The minima are slightly more pronounced in DK than in NT but are correlated in time, suggesting that these features are related to a large-scale cooling and drying pattern occurring in the ASMA. We also note that a layer of high H_2O rises to high altitudes (70-85 hPa) after 3 August (panel f), forming the local maximum above the CPT which we also find in our DK17 measurements (Figure 1e). This feature is remarkable and not in accordance with more typical climatological conditions observed during $NT16_{AUG}$.

Based on Figure 3, we argue that the differences between the $NT16_{AUG}$ and DK17 datasets are not due to local meteorological effects, which appear to have negligible impact on the UTLS temperature and H_2O at the two measurement sites. Rather, these differences are to be attributed to interannual variability, and in particular to a period of anomalously cold and dry UTLS at the southern slopes of the Himalayas, occurring after 3 August 2017 and persisting on a large scale.

5. UTLS structure during the ASM season

In this section we focus on analyzing the UTLS structure of the $NT16_{AUG}$ and DK17 measurements. The $NT16_{NOV}$ measurements will be discussed again in Section 6.

5.1 Asian tropopause transition layer (ATTL)

In the tropics, the thermodynamic transition between the troposphere and the stratosphere occurs over a layer of several kilometers in thickness, known as tropical tropopause layer (TTL). This layer is influenced by both upper tropospheric and lower stratospheric processes, and its properties control water vapor transport through the tropopause (e.g. Fueglistaler et al., 2009; Randel and Jensen, 2013). Amongst several different definitions of TTL used in the literature, reviewed by Pan et al. (2014), Gettelman and de F. Forster (2002) identify its boundaries based on the temperature and potential temperature lapse rates only, which is particularly suited for balloon-borne measurements. In their definition, the upper boundary of the TTL is the CPT, and the lower boundary the lapse rate minimum (LRM), i.e. the point in altitude where the change of potential temperature (θ) with altitude (z) is minimum. This defines the TTL as the layer in which the temperature lapse rate switches from convectively-dominated in the troposphere (small $d\theta/dz$, low stability), to radiatively-controlled in the stratosphere (high $d\theta/dz$, high stability) (Gettelman and de F. Forster, 2002). In addition, the LRM coincides with the mean convective outflow level (e.g. Gettelman and de F. Forster, 2002; Vömel et al. 2002; Paulik and Birner, 2012). Given the similarity between the UTLS region at the southern slopes of the Himalayas during the ASM season and that of the tropics, here we adopt this definition of TTL to study the thermal structure of our $NT16_{AUG}$ and DK17 datasets. However, being our measurement sites not tropical in a geographic sense, we refer to the TTL in this region and season as the Asian tropopause transition layer (ATTL).

Figure 4 shows mean profiles and standard deviations of $d\theta/dz$ as a function of pressure for the two ASM season datasets. The average LRM is found at lower pressure in DK17 compared to $NT16_{AUG}$ (169.5 vs 180 hPa), corresponding to roughly 400 m altitude difference, and the minimum in $d\theta/dz$ of DK17 is more pronounced (1.5 vs. 2 K/km). This suggests that, on average, convection reached higher altitudes in the ASM 2017 compared to 2016 at the southern slopes of the Himalayas, at least during the time of our measurements. The average ATTL boundaries in terms of pressure (potential temperature) are 180-97.5 hPa (360-382 K) for $NT16_{AUG}$, and 169.5-88 hPa (362.5-383.5 K) for DK17 (see Table 3: note that the data are binned with respect to pressure and the given potential temperature values are the average θ in the pressure levels where the LRM and CPT occur). We also observe that, due to the colder temperatures, the isentropic levels in DK17 are shifted to lower pressures compared to

$NT16_{AUG}$ (see Figure S4 in supplementary material), so that the large altitude difference between the two LRM and CPTs in $NT16_{AUG}$ compared to DK17 (400-600 m) becomes small in isentropic coordinates (1.5-2 K).

5.2 Confined lower stratosphere (CLS)

Since the anticyclonic circulation extends up to above the CPT, it is important for interpreting the observed vertical gradients of chemical species and aerosols to quantify the vertical extent of ASMA in the lower stratosphere. Here we estimate the top of the horizontal confinement effect of ASMA during the $NT16_{AUG}$ and DK17 campaign periods by means of air mass trajectories. For this, we consider 2-weeks LAGRANTO backward trajectories initialized at 5 hPa intervals between 40-150 hPa at the time of each balloon sounding in $NT16_{AUG}$ and DK17 (i.e. same as in Figures 2b, 2f, for 100 hPa), and 6 h before and 6 h after each sounding, using ERA-Interim wind fields. For each pressure level, we calculate the “confined fraction” of trajectories, defined as the fraction of trajectories which were already located inside the anticyclone 2 weeks before the measurements. For this purpose, based on the average geopotential height fields shown in Figures 2, we approximate the ASMA area as the box of 10-50°N latitude, 0-140°E longitude (see white dashed rectangle in Figures 2b, 2f).

Figure 5 shows the resulting confined fractions for $NT16_{AUG}$ and DK17 as a function of pressure. In both campaign periods, the confined fraction is high (above 60%) up to 70-80 hPa, while above it sharply decreases to zero. Confinement is higher for DK17 than for $NT16_{AUG}$ throughout the entire UTLS, which is qualitatively consistent with the backward trajectories shown in Figure 2. Based on these curves, we define the top of confinement (TOC) as the level of confined fraction = 50%, corresponding to 73 hPa in $NT16_{AUG}$ and 63.5 hPa in DK17. This level separates altitudes which are affected by horizontal confinement in ASMA (below TOC), from the confinement-free stratosphere above the ASMA (above TOC). Note that mean altitude and potential temperature levels of the TOC derived from the balloon measurements are given in Table 3.

Following from the definition of TOC, we further define the confined lower stratosphere (CLS) as the region of altitudes above the CPT and below the TOC. The CLS is the layer of lower stratosphere which is subject to confinement in ASMA, in contrast to the free stratosphere above the anticyclonic vortex (i.e. above TOC). Figure 6 illustrates the vertical structure of the UTLS above the southern slopes of the Himalayas during the ASM season according to the definitions of ATTL and CLS just introduced. In the following of this work, we refer to this framework of thermodynamically-significant levels and layers to discuss the vertical distributions and variability of water vapor, ozone, ice saturation and aerosols in ASMA.

5.3 Water vapor and ozone

To analyze our H_2O and O_3 measurements in relation to the thermodynamic structure of the UTLS, we define for each balloon sounding the altitude relative to the CPT as a new vertical coordinate. Figure 7 shows mean profiles and standard deviations of temperature, H_2O mixing ratio and O_3 mixing ratio in this coordinate system (note that, besides the CPT in black, the mean LRM and TOC levels are shown by blue dashed lines for $NT16_{AUG}$ and red dashed lines for DK17). Figure 8 shows probability density functions (PDFs) of temperature (left column), H_2O mixing ratio (center) and O_3 mixing ratio (right column) calculated in the free stratosphere (panels a-c), CLS (d-f), ATTL (g-i) and troposphere (j-l) regions, for $NT16_{AUG}$ and DK17. The PDFs of the free stratosphere region are calculated for altitudes between TOC and CPT + 5 km, while the troposphere PDFs between CPT – 6 km and LRM, i.e. covering the whole range of altitudes (with respect to CPT) as shown in Figure 7.

Water vapor mixing ratio in DK17 shows a minimum at the CPT and a local maximum in the CLS (Figure 7b), centered about 1 km above the local CPT (i.e. not the average CPT, but evaluated for each profile individually). The H_2O minimum is conceivably due to unusually high frequency of occurrence of ice clouds near the CPT in DK17, depleting water vapor from the gas phase in favor of the condensed phase, hence resulting in a strongly dehydrated CPT (see Section 5.4). The isolated H_2O maximum in the CLS is consistent with hydration by overshooting convective updrafts, injecting ice crystals above the CPT, which then evaporate and thus release localized "pockets" of moist air. Convective updrafts overshooting the CPT were observed by Corti et al. (2008), and a similar hydration mechanism was hypothesized by Dauhut et al. (2015; 2016).

In both $NT16_{AUG}$ and DK17, the PDFs of H_2O mixing ratio show higher water vapor in the CLS (Figure 8e) compared to the free stratosphere (Figure 8b). In particular, the PDFs in the CLS are broad (3-7 ppmv) and skewed towards high values, while the PDFs in the free stratosphere are narrow (3-5 ppmv) and show the expected distribution of background stratospheric water vapor. The high H_2O mixing ratios in the CLS in DK17 are obviously related to the previously discussed isolated maximum, yet enhanced frequency of occurrence of high H_2O mixing ratios is also observed in $NT16_{AUG}$, despite no local maximum was found in this dataset. This is consistent with the slow ascent of moist convective outflow air within the confined anticyclone, and in part may reflect the decreasing frequency of overshooting convective tops with altitude in $NT16_{AUG}$.

Ozone mixing ratio in DK17 shows a minimum slightly above the LRM (Figure 7c), which is characteristic of deep convection, rapidly transporting ozone-poor air from the boundary layer to the convective outflow level (e.g. Gettelman and de F. Forster, 2002; Vömel et al. 2002; Paulik and Birner, 2012). The absence of this feature in $NT16_{AUG}$ suggests that the average age of air, meant as the time elapsed since the last interaction with deep convection, was higher in $NT16_{AUG}$ compared to DK17, such that the O_3 minimum is smeared out by mixing and additional photochemical production (which is ehnanced in ASMA due to the enrichment in ozone precursors: Gottschaldt et al., 2018). Higher dilution of the convective signature in $NT16_{AUG}$ vs. DK17 is also consistent with the absence on an H_2O maximum above the CPT in $NT16_{AUG}$ (Figure 7b), and with the higher frequency of occurrence of low O_3 mixing ratios in DK17 compared to $NT16_{AUG}$ in the ATTL and CLS (Figures 8f, 8i).

In summary, both the $NT16_{AUG}$ and DK17 datasets show evidence of deep convection extending into the CLS, i.e. up to 1.5-2 km above the CPT. Convective features, such as low O_3 in the ATTL and high H_2O in the CLS, are more pronounced in DK17 than in $NT16_{AUG}$, indicating that DK17 likely sampled fresh convective outflow more frequently than $NT16_{AUG}$. This is also consistent with the higher altitude of the LRM in DK17 compared to $NT16_{AUG}$ (Figure 4) and suggests that convective activity at the southern slopes of the Himalayas was more frequent during the ASM season 2017 than in 2016.

Transport to the CLS is likely a combination of different processes, including overshooting convection, slow diabatic ascent, as well as adiabatic transport from regions with higher CPT potential temperature in ASMA (discussed in Section 7). Although we do not quantitatively evaluate these processes, we argue that the horizontal confinement effect of ASMA plays an important role in shaping the vertical distributions of H_2O and O_3 above the CPT, by keeping the moist convective outflow horizontally confined (while it continues to rise slowly) and thereby increasing the frequency of occurrence of air parcels with high H_2O and low O_3 above the CPT. This is supported by the fact that differences in H_2O and O_3 between $NT16_{AUG}$ and DK17 vanish in the free stratosphere (Figure 8a-c), which is in agreement with our trajectory-based definition of TOC. Further analysis will be required to disentangle the relevance of the different transport processes mentioned above in moistening the CLS.

5.4 Ice saturation

Figure 9 shows mean profiles and standard deviations of ice saturation (panel a) and histograms of supersaturated fraction (b) as a function of altitude relative to CPT, and PDFs of ice saturation calculated for the troposphere, ATTL and CLS regions (c-e). As a result of colder temperatures (see Figure 7a), much higher and more persistent ice saturations were measured in DK17 than in $NT16_{AUG}$ throughout the entire ATTL. In both datasets, the average ice saturation is higher in the ATTL compared to the troposphere, and in DK17 it shows a pronounced maximum with average supersaturated conditions (i.e. more than 50% of the measurements reach $S_{ice} > 1$) in the 1.5 km directly below the CPT. In contrast, the supersaturated fraction is 10-15% in $NT16_{AUG}$ over the same range of altitude. The ATTL ice saturations and supersaturated fractions of $NT16_{AUG}$ are comparable with previous measurements in Lhasa and Kunming, China during 2009-2010 (Bian et al., 2012), while the measurements in DK17 range significantly higher. This suggests that the frequency of occurrence of cirrus clouds in the ASM season 2017 was unusually high, which is likely the reason for the H_2O minimum at the CPT observed in DK17 (Figure 7b). Interestingly, we also note that ice supersaturations in DK17 extend frequently into the CLS, with about 30% supersaturated fraction in the first 500 m above the CPT (Figures 9b-9c). This implies that, in overshooting convective updrafts, ice crystals can regularly penetrate the CPT as condensed phase (e.g. see Figure 10f) and hence efficiently hydrate the CLS.

6. Aerosol and cloud backscatter

In this section we analyze the aerosol and cloud backscatter measurements by COBALD, which have not been discussed so far. COBALD was originally designed to investigate ice cloud properties, including cirrus (e.g. Brabec et al., 2012; Cirisian et al., 2014) and polar stratospheric clouds (e.g. Engel et al., 2014), yet recent measurements from Lhasa, China were also used for in-situ detection of the ATAL aerosols (Vernier et al., 2015; 2018). Here we address both aspects.

Since the BSR of aerosol droplets is 1-2 orders of magnitude smaller than that of cirrus clouds, the characterization of ATAL requires cloud-filtering techniques to eliminate in-cloud measurements, and therefore a large dataset for a statistically-significant evaluation (e.g. 18 soundings are used in Vernier et al., 2015). We performed 17 COBALD soundings in $NT16_{AUG}$, but due to logistical constraints only 3 could be realized during the DK17 campaign, which furthermore mostly sampled cloudy conditions near the CPT. For this reason, a clear-sky aerosol BSR profile cannot be established from the DK17 dataset. On the other hand, the 3 COBALD soundings available from $NT16_{NOV}$ are almost fully clear-sky measurements and therefore allow to calculate a clear-sky aerosol BSR profile. The $NT16_{NOV}$ measurements provide a useful reference state of background aerosols, without ASMA confinement and without supply of aerosols and precursor gases from the monsoonal deep convection, for comparison with $NT16_{AUG}$. In the following, we first provide an overview of the main characteristics of the observed cirrus clouds, and then detail the cloud-filtering technique and ATAL detection during the year 2016.

6.1 Cirrus clouds

Figure 10 shows individual soundings as examples of thin cirrus clouds observed during the $NT16_{AUG}$ (panels a-d) and DK17 (e-f) campaigns. Along with the temperature and ice saturation profiles, we show BSR at 455 nm (BSR_{455}), BSR at 940 nm (BSR_{940}), and color index (CI). Color index is defined as the 940-to-455 nm ratio of the aerosol component of BSR, i.e. CI = $(BSR_{940} - 1)/(BSR_{455} - 1)$. CI has the property of being independent of number density, hence it is a useful indicator of particle size (e.g. Cirisian et al., 2014) as long as particles are sufficiently small, so that Mie scattering oscillations are avoided. Based on the size-dependence of CI, considerations on the typical size range of ice crystals and aerosol droplets, and the evaluation of ice saturation measurements by CFH, a threshold of CI = 7 was empirically developed to discriminate in-cloud (CI > 7) from clear-sky measurements (CI < 7) (Vernier et al., 2015). This helps discerning the BSR features in Figure 10 as either ice cloud or aerosol signal, and is also used as a threshold for cloud-filtering. For example, in sounding NT004 (panel a), the sharp feature at 145 hPa with CI ≈ 10 is likely an ice cloud (note the concomitant ice supersaturation above the thin cloud layer, suggesting sedimentation), while the broad enhancement in BSR between 95-140 hPa without CI enhancement is the signal of ATAL. The main common characteristics of the cirrus clouds in Figure 10 is their very small spatial and optical thickness, with $BSR_{940} < 20$, while much larger values ($BSR_{940} \gg 100$) are expected in homogeneously-nucleated cirrus clouds, as often observed in the midlatitudes (e.g. Brabec et al., 2012; Cirisian et al., 2014), and as also shown by the thick outflow cirrus below 120 hPa in DK002 (panel f). Low BSR indicates low ice crystal number densities, suggesting that these clouds are most likely formed by heterogeneous nucleation on solid ice nuclei, rather than by homogeneous freezing of sulfate aerosol liquid droplets. This hypothesis is currently being investigated by a dedicated microphysical modeling study. Similarly thin cirrus clouds were observed in more than half of the COBALD soundings in $NT16_{AUG}$ (9 out of 17), therefore they occur very frequently in the ASMA, and they were often found embedded within the ATAL (Figure 10, panels a, e).

6.2 ATAL during the ASM season 2016

Figure 11 shows all clear-sky (i.e. aerosol only) BSR_{455} data points and mean profiles from the $NT16_{AUG}$ and $NT16_{NOV}$ datasets. Similarly to Vernier et al. (2015), the cloud-filtering criterion that we applied consists of three thresholds from two independent measurements, namely: $BSR_{940} < 2.5$ and CI < 7 from COBALD, and $S_{ice} < 0.7$ from CFH. Only data points which simultaneously fulfill all the three criteria above are classified as clear-sky and shown in Figure 11. The cloud-filtering method is illustrated by a scatter plot of BSR_{940} vs. CI given in Figure S5 in supplementary material.

In $NT16_{AUG}$, clear-sky BSR_{455} enhancement (i.e. mean value exceeding 1.04) starting approximately at the LRM (180 hPa) and extending up to the TOC (73 hPa) is the signature of ATAL (Figure 11), showing intensity and vertical extent comparable to those derived by satellite retrievals and previous COBALD measurements (Vernier et al., 2015; 2018). The enhanced aerosol BSR_{455} covers both the ATTL and the CLS, with maximum BSR_{455} at the CPT. The fact that ATAL's onset coincides with the LRM suggests that the mean convective outflow level is also the onset of horizontal confinement in ASMA. Maximum BSR_{455} at the CPT is possibly an effect of colder temperatures, driving the partitioning of more condensable material (e.g. nitrates, see Vernier et al., 2018) to the aerosol phase in ATAL. Above the CPT, the BSR_{455} enhancement gradually faints with altitude until the TOC as the horizontal confinement effect of ASMA vanishes, which is consistent with the decreasing confined fraction of backward trajectories shown in Figure 5. Above the TOC, the ATAL signal merges with the Junge layer of stratospheric aerosols, which extends into the free stratosphere up to about 10 hPa. The clear-sky BSR_{455} enhancement is absent in $NT16_{NOV}$ at all altitudes in the UTLS (except for the Junge layer in the free stratosphere), showing that ATAL does not outlive the break-up of the anticyclonic vortex and the lack of supply of precursor gases by deep convection after the end of the ASM season.

7. Discussion and conclusions

We analyzed 63 balloon measurements of temperature, water vapor, ozone and aerosol backscatter, collected during the years 2016-2017 at the southern slopes of the Himalayas. The UTLS structure in this region exhibits a strong seasonal variability, with tropical features (sharp CPT) during the ASM, and midlatitudinal features (large LRT-CPT separation) during the post-monsoon season. To analyze the structure of the UTLS during the ASM season, we formulate a framework composed of three thermodynamically significant levels (LRM, CPT, TOC) and two layers (ATTL, CLS) illustrated in Figure 6. Figure 12 summarizes the mean profiles of temperature, $d\theta/dz$, H_2O mixing ratio, O_3 mixing ratio, ice saturation and aerosol BSR_{455} measured during $NT16_{AUG}$ (top panel) and DK17 (bottom panel), highlighting the relevance of these levels and layers.

During both the ASM season campaigns, the isentropic level of the LRM (θ = 362-364 K) was higher than in previous measurements in the deep tropics ($\theta \approx$ 345 K) (Gettelman and de F. Forster, 2002; Pan et al., 2014) and in the Tibetan plateau (355-360 K) (Bian et al., 2012), suggesting that convection is very deep-penetrating at the southern slopes of the Himalayas. The CPT (θ = 382-384 K) was also higher than at tropical sites (375 K) (Gettelman and de F. Forster, 2002; Pan et al., 2014), but lower than in the Tibetan plateau (390 K) (Bian et al., 2012), which is consistent with the "bulging" of the CPT in ASMA (e.g. Pan et al., 2016) and suggests an orographic influence. The average LRM and CPT occur at higher altitude in DK17 compared to $NT16_{AUG}$ (400-600 m), but due to colder temperatures in DK17 (on average 5 K at the CPT), the shift in potential temperature space is small (1.5-2 K). We also note that in DK17 the TOC coincides with a local maximum in the thermal stability profile ($d\theta/dz$), which is the same feature as the level of maximum stability defined by Sunilkumar et al. (2017).

In both $NT16_{AUG}$ and DK17, high H_2O and low O_3 were found in the ATTL and CLS, which is the signature of deep convection, extending up to 1.5-2 km above the CPT. Convective features are more pronounced in DK17 compared to $NT16_{AUG}$, suggesting that convective activity at the southern slopes of the Himalayas was more intense during the ASM season 2017 compared to

2016. In particular, an isolated H_2O maximum in the CLS was observed in DK17, which we argue it may be due to overshooting convection, as previously observed by Corti et al. (2008) and modelled by Dauhut et al. (2015; 2016).

The fact that the average CPTs in our datasets occur at lower potential temperatures than previously found above the Tibetan plateau suggests that, in addition to slow ascent and overshooting convection (discussed in Section 5.3), isentropic transport from the Tibetan plateau (below CPT) to the southern slopes of the Himalayas (above CPT) might also contribute to the high H_2O observed in the CLS. Nevertheless, since the isentropic level of the CPT is subject to strong instantaneous perturbations associated with convection and wave activity (e.g. Boehm and Verlinde, 2000; Sherwood et al., 2003; Munchak and Pan, 2014; Muhsin et al., 2018), a conclusion based on just the average CPT from a limited number of profiles is to be taken with caution, and further investigations will be required to assess the relevance of the different transport pathways.

The high H_2O observed in the CLS is particularly interesting because of its potential implications for stratospheric moistening. The air masses in the CLS have already crossed the CPT, hence will be unlikely subject to further dehydration, so it appears that the high H_2O in this layer is prone to be lifted further and mixed into the (drier) free stratosphere. However, it was shown that vertical transport above the ASMA might not be very efficient due to the slow ascending velocities of the Brewer-Dobson circulation in this region and season, and that the most efficient transport pathway is quasi-horizontal transport through the horizontal boundaries of ASMA and subsequent upwelling in the stratosphere above the deep tropics (Pan et al., 2016). Therefore, the fate of the air masses in the CLS (hence the moistening potential of the high H_2O in this layer) needs to be addressed by explicitly taking into account the horizontal motion of the air, which we do not investigate in this work.

Cloud-filtering of the $NT16_{AUG}$ aerosol backscatter measurements reveals the signature of ATAL, extending from the LRM to the TOC with maximum backscatter at the CPT, and with similar BSR enhancement as in previous measurements from Lhasa, China (Vernier et al., 2015). No aerosol enhancement was found in $NT16_{NOV}$. In both $NT16_{AUG}$ and DK17, ice saturation is minimum at the LRM and increases in the ATTL, similarly to as in the tropics (Vömel et al., 2002). Due to the much colder temperatures, average S_{ice} in DK17 is remarkably higher than in $NT16_{AUG}$, as well as than in previous measurements from the Tibetan plateau (Bian et al., 2012). Numerous thin cirrus clouds were detected during the $NT16_{AUG}$ and DK17campaigns (often embedded in ATAL), and their optical properties suggest they might be formed by heterogeneous freezing.

Our analysis provides a comprehensive and high-resolution overview of the UTLS structure and composition at the southern slopes of the Himalayas. The thermodynamically-significant levels and layers that we identify offer physically-meaningful boundaries for the interpretation of the observed vertical distributions of water vapor, ozone and aerosols in ASMA, and the extents of enhanced H_2O and aerosols (ATAL) above the CPT are in good agreement with the top of anticyclonic confinement estimated from air mass backward trajectories. Our approach based on significant levels, rather than fixed pressure or altitude stacks, also provides useful diagnostics for the comparison of our in-situ measurements with global climate model outputs.

As often mentioned throughout the paper, a wide range of modeling, interpretation and comparison studies are ongoing, aiming to explore all the different insights offered by this dataset, and to assess its relevance in the context of stratospheric moistening via the ASMA system and related transport pathways. These investigations include microphysical modeling, Lagrangian trajectory analyses, instrumental studies and comparisons with other in-situ measurements, such as the airborne measurements of Geophysica-M55 during the StratoClim 2017 aircraft campaign and balloon soundings performed from various stations in the Tibetan plateau during the years 2013-2017, as well as comparisons with different global modeling products.

References

Bergman, J. W., Fierli, F., Jensen, E. J., Honomichl, S., and Pan, L. L.: Boundary layer sources for the Asian anticyclone: Regional contributions to a vertical conduit, J. Geophys. Res. Atmos., 118, 2560-2575, doi:10.1002/jgrd.50142, 2013

Bian, J., Pan, L. L., Paulik, L., Vömel, H., Chen, H, and Lu, D.: In situ water vapor measurements in Lhasa and Kunming during the Asian summer monsoon, Geophys. Res. Lett., 39, L19808, doi:10.1029/2012GL052996, 2012

Boehm, M. T., and Verlinde, J.: Stratospheric influence on upper tropospheric tropical cirrus, Geophys. Res. Lett., 27, 19, 3209-3212, 2000

Brabec, M., Wienhold, F. G., Luo, B. P., Vömel, H., Immler, F., Steiner, P., Hausammann, E., Weers, U. and Peter, T.: Particle backscatter and relative humidity measured across cirrus clouds and comparison with microphysical cirrus modelling, Atmos. Chem. Phys., 12, 9135-9148, doi:10.5194/acp-12-9135-2012, 2012

Bucholtz, A.: Rayleigh-scattering calculations for the terrestrial atmosphere, Appl. Optics, 34, 15, 1995

Cirisian, A., Luo, B. P., Engel, I., Wienhold, F. G., Sprenger, M., Krieger, U. K., Weers, U., Romanens, G., Levrat, G., Jeannet, P., Ruffiex, D., Philipona, R., Calpini, B., Spichtinger, P. and Peter, T.: Balloon-borne measurements of milatitude cirrus clouds, Atmos. Chem. Phys., 14, 7341-7365, doi:10.5194/acp-14-7341-2014, 2014

Corti, T., Luo, B. P., de Reus, M., Brunner, D., Cairo, F., Mahoney, M. J., Martucci, G., Matthey, R., Mitev, V., dos Santos, F. H., Schiller, C., Shur, G., Sitnikov, N. M., Spelten, N., Vössing, H. J., Borrmann, S., and Peter, T.: Unprecedented evidence for deep convection hydrating the tropical stratoshpere, Geophys. Res. Lett., 35, L10810, doi:10.1029/2008GL033641, 2008

Dauhut, T., Chaboureau, J.-P., Escobar, J., and Mascart, P.: Large-eddy simulations of Hector the convector making the stratosphere wetter, Atmos. Sci. Lett., 16, 135-140, DOI:10.1002/asl2.534, 2015

Dauhut, T., Chaboureau, J.-P., Escobar, J., and Mascart, P.: Giga-LES of Hector the Convector and Its Two Tallest Updrafts up to the Stratosphere, J. Atmos. Sci., 73, 5041-5060, DOI:10.1175/JAS-D-16-0083.1, 2016

Dethof, A., O'Neill, A., Slingo, J. M., and Smit, H. G. J.: A mechanism for moistening the lower stratosphere involving the Asian summer monsoon, Q. J. R, Meteorol. Soc., 125, 1079-1106, 1999

Engel, I., Luo, B. P., Khaykin, S. M., Wienhold, F. G., Vömel, H., Kivi, R., Hoyle, C. R., Gross, J.-U., Pitts, M. C., and Peter, T.: Arctic stratospheric dehydration - Part 2: Microphysical modeling, Atmos. Chem. Phys., 14, 3231-3246, doi:10.5194/acp-14-3231-2014, 2014

Fadnavis, S., Semeniuk, K., Pozzoli, L., Schultz, M. G., Ghude, S. D., Das, S., and Kakaktar, R.: Transport of aerosols into the UTLS and their impact on the Asian monsoon region as seen in a global model simulation, Atmos. Chem. Phys., 13, 8771-8786, doi:10.5194/acp-13-8771-2013, 2013

Fadnavis, S., Schultz, M. G., Semeniuk, K., Mahajan, A. S., Pozzoli, L., Sonbawne, S., Ghude, S. D., Kiefer, M., and Eckert, E.: Trends in peroxyacetyl nitrate (PAN) in the upper troposphere and lower stratosphere over southern Asia during the summer monsoon season: regional impacts, Atmos. Chem. Phys., 14, 12725-12743, doi.org/10.5194/acp-14-12725-2014, 2014

Fu, R., Hu, Y., Wright, J. S., Jiang, J. E., Dickinson, R. E., Chen, M., Filipiak, M., Read, W. G., Waters, J. W., and Wu, D. L.: Short circuit of water vapor and polluted air to the global stratosphere by convective transport over the Tibetan plateau, Proc. Natl. Acad. Sci. USA, 103, 15, 5664, doi:10.1073_pnas.0601584103, 2006

Fueglistaler, S., Dessler, A. E., Dunkerton, T. J., Folkins, I., Fu, Q., and Mote, P. W.: Tropical tropopause layer, Rev. Geophys., 47, RG1004, doi:10.1029/2008RG000267, 2009

Garny, H. and Randel, W.: Dynamic variability of the Asian monsoon anticyclone observed in potential vorticity and correlations with tracer distributions, J. Geophys. Res. Atmos., 118, 13421-13433, doi:10.1002/2013JD020908, 2013

Garny, H. and Randel, W.: Transport pathways from the Asian monsoon anticyclone to the stratosphere, Atmos. Chem. Phys., 16, 2703-2718, doi:10.5194/acp-16-2703-2016, 2016

Gettelman, A. and de F. Forster, P. M.: A climatology of the Tropical Tropopause Layer, J. Meteorol. Soc. Japan, 80, 911-924, 2002

Gottschaldt, K.-D., Schlager, H., Baumann, R., Sinh Cai, D., Eyring, V., Graf, P., Grewe, V., Jöckel, P., Jurkat-Witschas, T., Voigt, C., Zahn, A., and Ziereis, H.: Dynamics and composition of the Asian summer monsoon anticyclone, Atmos. Chem. Phys., 18, 5655-5675, http://doi.org/10.5194/acp-18-5655-2018, 2018

Heath, N. K. and Fuelberg, H. E.: Using a WRF simulation to examine regions where convection impacts the Asian monsoon anticyclone, Atmos. Chem. Phys., 14, 2055-2070, doi:10.5194/acp-14-2055-2014, 2014

Hoskins, B. J., and Rodwell, M. J.: A Model of the Asian Summer Monsoon. Part I: The Global Scale, J. Atmos. Sci., 52, 1329-1340, 1995

InterMet: iMet-1-RS 403 MHz Research Radiosonde, Data Sheet, International Met Sytems, 3854 Broadmoore SE, Grand Rapids, MI, USA, http://www.intermetsystems.com/ee/pdf/iMet-1_RS_Data_130530.pdf, 2006 (accessed 4 January 2018)

Jordan, A. and Hall, E.: SkySonde User Manual, Version 1.9, ftp://aftp.cmdl.noaa.gov/user/jordan/Sky-Sonde%20User%20Manual.pdf, 2016 (accessed 4 January 2018)

Komhyr, W. D.: Electrochemical Concentration Cells for gas analysis, Ann. Geophys., 25, 203-210, 1969

Kräuchi, A., Philipona, R., Romanens, G., Hurst, D. F., Hall, E. G., and Jordan, A. F.: Controlled weather balloon ascents and descents for atmospheric research and climate monitoring, Atmos. Meas. Tech., 9, 929-938, doi:10.5194/amt-9-929-2016, 2016

Krishnamurti, T. N. and Bhalme, H. N.: Oscillations of a Monsoon System. Part I. Observational Aspects, J. Atmospheric Sci., 33, 1937-1954, 1976

Krotkov, N. A., McLinden, C. A., Li, C., Lamsal, L. N., Celarier, E. A., Marchenko, S. V., Swartz, W. H., Bucsela, E. J., Joiner, J., Buncan, B. N., Boersma, F. K., Veefkind, P. J., Levelt, P. F., Fioletov, V. E., Dickerson, R. R., He, H., Lu, Z., and Streets, D. G.: Aura OMI observations of regional SO_2 and NO_2 pollution changes from 2005 to 2015 et al. (2016), Atmos. Chem. Phys., 16, 4605-4629, doi:10.5194/acp-16-4605-2016, 2016

Kumar, R., Naja, M., Venkataramani, S., and Wild, O.: Variations in surface ozone at Nainital: A high-altitude site in the central Himalays, J. Geophys. Res., 115, D16302, doi:10.1029/2009JD013715, 2010

Kunz, A., Konopka, P., Müller, R., and Pan, L. L.: Dynamical tropopause based on isentropic potential vorticity gradients, J. Geophys. Res., 116, D01110, doi:10.1029/2010JD014343, 2011

Lawrence, M. G., and Lelieveld, J.: Atmospheric pollutant outflow from southern Asia: a review, Atmos. Chem. Phys., 10, 11017-11096, doi:10.5194/acp-10-11017-2010, 2010

Muhsin, M., Sunilkumar, S. V., Venkat Ratnam, M., Parameswaran, K., Krishna Murthy, B., and Emmanuel, M.: Effect of convection on the thermal structure of the troposphere and lower stratosphere including the tropical tropopause layer in the South Asian monsoon region, J. Atmospheric Sol.-Terr. Phys., 169, 52-65, https://doi.org/10.1016/j.jastp.2018.10.016, 2018

Munchak, L. A., and Pan, L. L., Separation of the lapse rate and the cold point tropopauses in the tropics and the resulting impact on cloud top-tropopause relationships, J. Geophys. Res. Atmos., 119, 7963-7978, doi:10.1002/2013JD021189, 2014

Murphy, D. M. and Koop, T.: Review of the vapour pressures of ice and supercooled water for atmospheric applications, Q. J. R, Meteorol. Soc, 131, 1539-1565, doi:10.1256/qj.04.94, 2005

Nützel, M., Dameris, M., and Garny, H.: Movements, drivers and bimodality of the South Asian High, Atmos. Chem. Phys., 16, 14755-14774, doi:10.5194/acp-16-14755-2016, 2016

Oelsner, P. and Tietz, R.: GRUAN Monitor MW41 and the Vaisala RS41 Additional Sensor Interface, Technical Note 8 (GRUAN-TN-8), https://www.gruan.org/gruan/editor/documents/gruan/GRUAN-TN-8_GRUAN-Monitor-MW41-and-Vaisala_RS41_Additional_Sensor_Interface_v1.0.pdf, 2017 (accessed 4 January 2018)

Orbe, C., Waugh, D. W., and Newman, P. A.: Air-mass origin in the tropical lower stratosphere: The influence of Asian boundary layer air, Geophys. Res. Lett., 42, 4240-4248, https://doi.org/10.1002/2015GL063937, 2015

Pan, L. L., Paulik, L. C., Honomichl, S. B., Munchak, L. A., Bian, J., Selkirk, H. B., and Vömel, H.: Identification of the tropical tropopause transition layer using the ozone - water vapor relationship, J. Geophys. Res. Atmos., 119, 3586-3599, doi:10.1002/2013JD020558, 2014

Pan, L. L., Honomichl, S. B., Kinnison, D. E., Abalos, M., Randel, W. J., Bergman, J. W., and Bian, J.: Transport of chemical tracers from the boundary layer to stratosphere associated with the dynamics of the Asian summer monsoon, J. Geophys. Res. Atmos., 121, 14159-14174, doi:10.1002/2016JD025616, 2016

Park, M., Randel, W. J., Kinnison, D. E., Garcia, R. R., and Choi, W.: Seasonal variation of methane, water vapor, and nitrogen oxides near the tropopause: Satellite observations and model simulations, J. Geophys. Res., 109, D03302, doi:10.1029/2003JD003706, 2004

Park, M., Randel, W. J., Gettelman, A., Massie, S. T., and Jiang, J. H.: Transport above the Asian summer monsoon anticyclone inferred from Aura Microwave Limb Sounder tracers, J. Geophys. Res., 112, D16309, doi:10.1029/2006JD008294, 2007

Park, M., Randel, W. J., Emmons, L. K., Bernath, P. F., Walker, K. A., and Boone, C. D.: Chemical isolation in the Asian monsoon anticyclone observed in Atmospheric Chemistry Experiment (ACE-FTS) data, Atmos. Chem. Phys., 8, 757-764, www.atmos-chem-phys.net/8/757/2008/, 2008

Paulik, L. C. and Birner, T.: Quantifying the deep convective temperature signal within the tropical tropopause layer (TTL), Atmos. Chem. Phys., 12, 12183-12195, doi:10.5194/acp-12-12183-2012, 2012

Ploeger, F., Gottschling, C., Griessbach, S., Gross, J.-U., Guenther, G., Konopka, P., Müller, R., Riese, M., Stroh, F., Tao, M., Ungermann, J., Vogel, B., and von Hobe, M.: A potential vorticity-based determination of the transport barrier in the Asian summer monsoon anticyclone, Atmos. Chem. Phys., 15, 13145-13159, doi:10.5194/acp-15-13145-2015, 2015

Randel, W. J. and Park, M.: Deep convective influence on the Asian summer monsoon anticyclone and associated tracer variability observed with Atmospheric Infrared Sounder (AIRS), J. Geophys. Res., 111, D12314, doi:10.1029/2005JD006490, 2006

Randel, W. J., Wu, F., Gettelman, A., Russel III, J. M., Zawodny, J. M., and Oltmans, S. J.: Seasonal variation of water vapor in the lower stratosphere observed in Halogen Occultation Experiment data, J. Geophys. Res., 106, 14313-14325, JD900048509.00, 2001

Randel, W., Udelhofen, P., Fleming, E., Geller, M., Gelman, M., Hamilton, K., Karoly, D., Ortland, D., Pawson, S., Swinbank, R. Wu, F., Baldwin, M., Chanin, M. L., Keckhut, P., Labitzke, K., Remsberg, E., Simmons, E., and Wu, D.: The SPARC Intercomparison of Middle-Atmosphere Climatologies, J. Clim., 17, 986-1003, 2003

Randel, W. J., Park, M., Emmons, L., Kinnison, D., Bernath, P., Walker, K. A., Boone, C., and Pumphrey, H.: Asian Monsoon Transport of Pollution to the Stratosphere, Science, 328, 611-613, doi:10.1126/science.1182274, 2010

Randel, W. J., and Jensen, E. J.: Physical processes in the tropical tropopause layer and their roles in a changing climate, Nat. Geosci., 6, 169-176, DOI:10.1038/NGEO1733, 2013

Rauthe-Schöch, A., Baker, A. K., Schuck, T. J., Brenninkmejer, C. A. M., Zahn, A., Hermann, M., Stramann, G., Ziereis, H., van Velthoven, P. F. J., and Lelieveld, J.: Trapping, chemistry and export of trace gases in the South Asian summer monsoon observed during CARIBIC flights in 2008, Atmos. Chem. Phys., 16, 3609-3629, doi:10.5194/acp-16-3609-2016, 2016

Rosen, J. M. and Kjome, N. T.: Backscattersonde: a new instrument for atmospheric aerosol research, Applied Optics, 30, 12, 1552-1561, 1991

Sherwood, S. C., Horinouhi, T., and Zeleznik, H. A.: Convective Impact on Temperatures Observed near the Tropical Tropopause, J. Atmos. Sci., 60, 1847-1855, 2003

Smit, H. G. J., Straeter, W., Johnson, B. J., Oltmans, S. J., Davies, J., Tarasick, D. W., Hoegger, B., Stubi, R., Schmidlin, F. J., Northam, T., Thompson, A. M., Witte, J. C., Boyd, I., and Posny, F.: Assessment of the performance of ECC-ozonesondes under quasi-flight conditions in the environmental simulation chamber: Insights from the Juelich Ozone Sonde Intercomparison Experiment (JOSIE), J. Geophys. Res., 112, D19306, doi:10.1029/2006JD007308, 2007

Sunilkumar, S. V., Muhsin, M., Venkat Ratnam, M., Parameswaran, K., Krishna Murthy, B. V., and Emmanuel, M.: Boundaries of tropical tropopause layer (TTL): A new perspective based on thermal and stability profiles, J. Geophys. Res. Atmos., 122, 741-754, doi:10.1002/2016JD025217, 2017

Thomason, L. W. and Vernier, J.-P.: Improved SAGE II cloud/aerosol categorization and observations of the Asian tropopause aerosol layer: 1989-2005, Atmos. Chem. Phys., 13, 4605-4616, doi:10.5194/acp-13-4605-2013, 2013

Ungermann, J., Ern, M., Kaufmann, M., Müller, R., Spang, R., Ploeger, F., Vogel, B., and Riese, M.: Observations of PAN and its confinement in the Asian summer monsoon anticyclone in high spatial resolution, Atmos. Chem. Phys., 16, 8389-8403, doi:10.5194/acp-16-8389-2016, 2016

Vaisala: Vaisala DigiCORA Sounding System MW41, Technical Reference, Vaisala Oyi, P.O. Box 26, Fl 00421, Helsinki, Finland, http://meteorology.lyndonstate.edu-/ATM/wp-content/uploads/2015/05/M211415EN-F.pdf, 2014 (accessed 4 January 2018)

Vaisala: Vaisala Radiosonde RS41 Measurement Performance, White Paper, Vaisala, P.O. Box 26, Fl 00421, Helsinki, Finland, https://www.vaisala.com/sites/default/files/documents/WEA-MET-RS41-Performance-White-paper-B211356EN-B-LOW-v3.pdf, 2017 (accessed 4 January 2018)

Vellore, R. K., Kaplan, M. L., Krishnan, R., Lewis, J. M., Sabade, S., Deshpande, N., Singh, B. B., Madhura, D. K., and Rama Rao, S. V. S.: Monsoon-extratropical circulation interactions in Himalayan extreme rainfall, Clim. Dyn., 46, 3517-3546, doi:10.1007/s00382-015-2784-x, 2016

Vernier, J.-P., Thomason, L. W., and Kar, J.: CALIPSO detection of an Asian tropopause aerosol layer, Geophys. Res. Lett., 38, L07804, doi:10.1029/2010GL046614, 2011

Vernier, J.-P., Fairlie, T. D., Natarajan, M., Wienhold, F. G., Bian, J., Martinsson, B. G., Crumeyrolle, S., Thomason, L. W., and Bedka, K. M.: Increase in upper tropospheric and lower stratospheric aerosol levels and its potential connection with Asian pollution, J. Geophys. Res. Atmos., 120, 1608-1619, doi:10.1002/2014JD022372, 2015

Vernier, J.-P., Fairlie, T. D., Deshler, T., Venkat Ratnam, M., Gadhavi, H., Kumar, B. S., Natarajan, M., Pandit, A. K., Akhil Raj, S. T., Hemanth Kumar, A., Jayaraman, A., Singh, A. K., Rastogi, N., Sinha, P. R., Kumar, S., Tiwari, S., Wegner, T., Baker, N., Vignelles, D., Stenchikov, G., Shevchenko, I., Smith, J., Bedka, K., Kesarkar, A., Singh, V., Bhate, J., Ravikiran, V., Durga Rao, M., Ravindrababu, S., Patel, A., Vernier, H., Wienhold, F. G., Liu, H., Knepp, T. N., Thomason, L., Crawford, J., Ziemba, L., Moore, J., Crumeyrolle, S., Williamson, M., Berthet, G., Jégou, F., and Renard, J.-B.: BATAL The Balloon Measurement Campaigns of the Asian Tropopause Aerosol Layer, Bull. Am. Meteorol. Soc., May 2018, 955-973, https://doi.org/10.1175/BAMS-D-17-0014.1, 2018

Vogel, B., Günther, G., Müller, R., Gross, J.-U., Hoor, P., Krämer, M., Müller, S., Zahn, A., and Riese, M.: Fast transport from Southeast Asia boundary layer sources to Nothern Europe: rapid uplift in typhoons and eastward eddy shedding of the Asian monsoon anticyclone, Atmos. Chem. Phys., 14, 12745-12762, https://doi.org/10.5194/acp-14-12745-2014, 2014

Vogel, B., Günther, G., Müller, R., Gross, J.-U., and Riese, M.: Impact of different Asian source regions on the composition of the Asian monsoon anticyclone and of the etratropical lowermost stratosphere, Atmospheric Chemistry and Physics, 15, 13699-13716, doi:10.5194/acp-15-13699-2015, 2015

Vömel, H., Oltmans, S. J., Johnson, B. J., Hasebe, F., Shiotani, M., Fujiwara, M., Nishi, N., Agama, M., Cornejo, J., Paredes, F. and Enriquez, H.: Balloon-borne observations of water vapor and ozone in the tropical upper troposphere and lower stratosphere, J. Geophys. Res., 107, D14, 4210, doi: 10.1029/2001JD000707, 2002

Vömel, H., David, D. E., and Smith, K.: Accuracy of tropospheric and stratospheric water vapor measurements by the cryogenic frost point hygrometer: Instrumental details and observations, J. Geophys. Res., 112, D08305, doi:10.1029/2006JD007224, 2007

Vömel, H., Naebert, T., Dirksen, R., and Sommer, M.: An update on the uncertainties of water vapor measurements using Cryogenic Frostpoint Hygrometers, Atmos. Meas. Tech., 9, 3755-3768, https://doi.org/10.5194/amt-9-3755-2016, 2016

Wendell, J. and Jordan, A.: iMet-1-RSB Radiosonde XDATA Protocol & Daisy Chaining, version 1.3, ftp://aftp.cmdl.noaa.gov/user/jordan/iMet-1-RSB%20Radiosonde%20XDATA%20Daisy%20Chaining.pdf, 2016 (accessed 4 January 2018)

Wernli, H. and Davies, H. C.: A Lagrangian-based analysis of extratropical cyclones. I: The method and some applications, Q. J. R. Meteorol. Soc., 123, 467-489, 1997

World Meteorological Organization (WMO): Meteorology – A three-dimensional science: Second session of the commission for aerology, World Meteorol. Organ. Bull., 4, 134-138, 1957

Yan, R. C., Bian, J., and Fan, Q. J.: The Impact of the South Asia High Bimodality on the Chemical Composition of the Upper Troposphere and Lower Stratosphere, Atmos. Ocean. Sci. Lett., 4, 229-234, 2011

Acknowledgements

The research leading to these results has received funding from the European Community's Seventh Framework Programme (FP7/2007 - 2013) under grant agreement n° 603557 and the Swiss National Science Foundation in project n° 200021-117987. The use of ECMWF operational and ERA-Interim data is gratefully acknowledged. Support from the Director ARIES and the ISRO ATCTM project is highly acknowledged for the observations at Nainital. Support from the HiCCDRC group of Kathmandu University is highly acknowledged for the observations at Dhulikhel. Maxi Boettcher acknowledges funding from the Swiss National Science Foundation via grant 200020-165941. The author Simone Brunamonti thanks Dr. Federico Fierli and Dr. Laura Pan for inspiring discussion.

Acronym	Description
Thermodynamic structure and features	
ASM	Asian summer monsoon
ASMA	Asian summer monsoon anticyclone
ATAL	Asian tropopause aerosol layer
ATTL	Asian tropopause transition layer
CLS	Confined lower stratosphere
CPT	Cold-point tropopause
LRM	Lapse-rate minimum
LRT	Lapse-rate tropopause
TOC	Top of confinement
UTLS	Upper troposphere - lower stratosphere
Measurement sites	
NT	Nainital, India (29.35°N, 79.46°E)
DK	Dhulikhel, Nepal (27.62°N, 85.54°E)
$NT16_{AUG}$	Balloon campaign in NT in August 2016
$NT16_{NOV}$	Balloon campaign in NT in November 2016
DK17	Balloon campaign in DK in July-August 2017

Table 1. List of the main acronyms used in this paper.

Campaign	Time period	RS41	ECC	CFH	COBALD	Early burst
$NT16_{AUG}$	2-31 Aug 2016	30* (0)	24 (2)	27 (1, 5)	17 (0)	4
$NT16_{NOV}$	2-8 Nov 2016	5 (0)	5 (0)	5 (0, 1)	3 (1)	0
DK17	30 Jul-12 Aug 2017	28 (0)	12 (2)	11 (0, 4)	3 (0)	5
Total		**63* (0)**	**41 (4)**	**43 (1, 10)**	**23 (1)**	**9**

Table 2. Number of balloon soundings performed for each instrument and campaign period. In parentheses: number of soundings with instrumental malfunctionings (CFH: number of failures and contamination events, respectively). Early burst is defined as burst altitude < 25 km. (*) Note that iMet radiosondes were used for the first two soundings in $NT16_{AUG}$, instead of RS41 (see Section 2).

	$NT16_{AUG}$				$NT16_{NOV}$				DK17			
	z **(km)**	***p*** **(hPa)**	***θ*** **(K)**	***T*** **(°C)**	***z*** **(km)**	***p*** **(hPa)**	***θ*** **(K)**	***T*** **(°C)**	***z*** **(km)**	***p*** **(hPa)**	***θ*** **(K)**	***T*** **(°C)**
LRM	13.3	180	360	-52.7	10.5	260	337.5	-43.6	13.7	169.5	362.5	-55
LRT	17.0	97.5	382	-76.8	16.0	108	378	-73.2	17.6	88	383.5	-81.7
CPT	17.0	97.5	382	-76.8	18.5	69.5	424	-75.3	17.6	88	383.5	-81.7
TOC	18.6	73	421.5	-73.7	*N.A.*	*N.A.*	*N.A.*	*N.A.*	19.5	63.5	441	-72.7

Table 3. Mean values of altitude (*z*), pressure (*p*), potential temperature (*θ*) and temperature (T) of the lapse rate minimum (LRM), lapse rate tropopause (LRT), cold-point tropopause (CPT) and top of confinement (TOC) levels during the three campaign periods, $NT16_{AUG}$, $NT16_{NOV}$ and DK17. Note that for $NT16_{NOV}$, the definition of TOC is not applicable (N.A.).

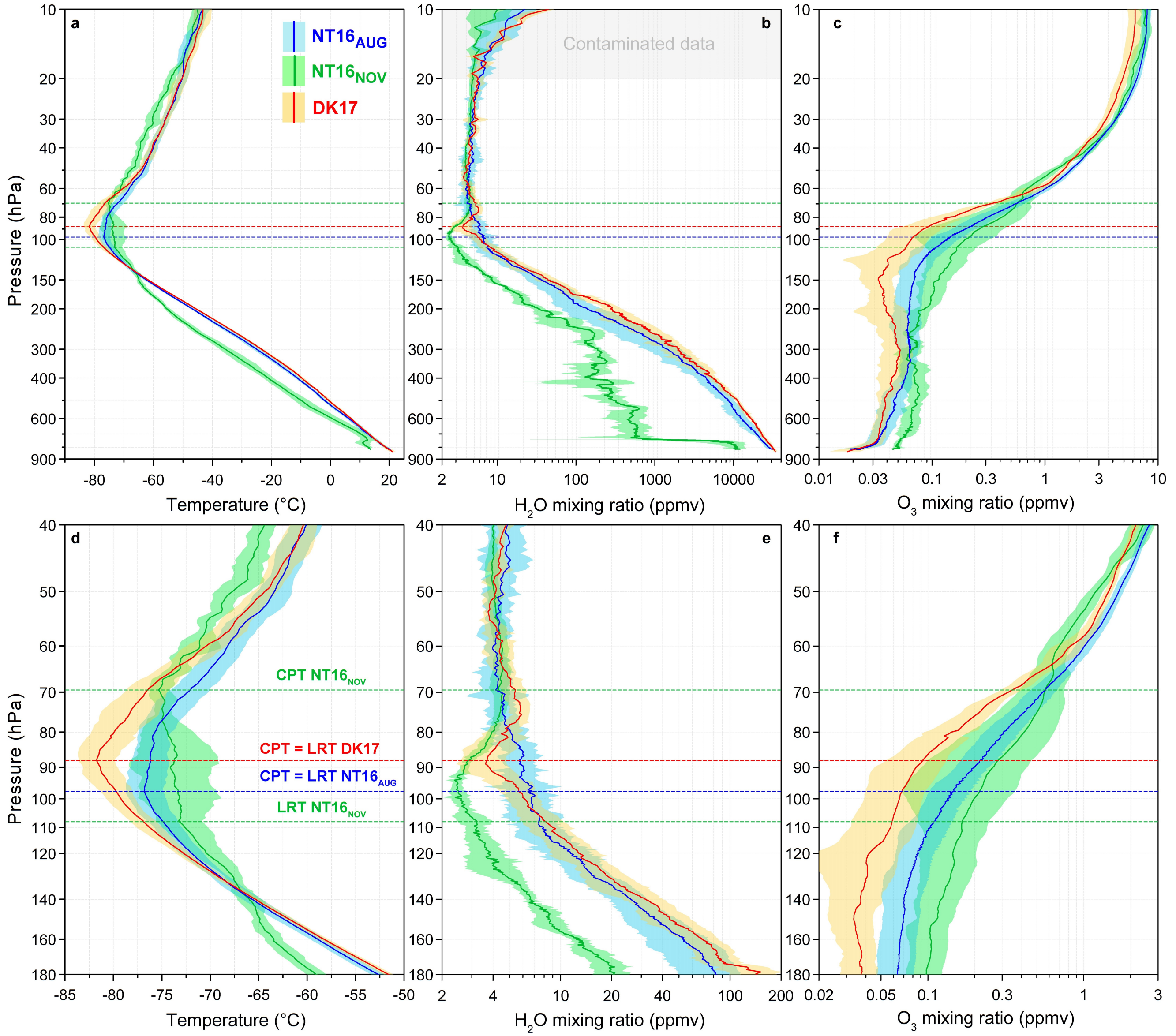

Figure 1. Mean profiles (solid lines) and standard deviations (color shading) of all measurements of temperature from RS41 (panels a, d), H_2O mixing ratio from CFH (b, e) and O_3 mixing ratio from ECC (c, f) as a function of pressure, for $NT16_{AUG}$ (blue), $NT16_{NOV}$ (green) and DK17 (red). Dashed lines indicate the pressure levels of the average cold-point tropopause (CPT) and lapse-rate tropopause (LRT) for the different datasets. Upper row (a-c): measured profiles from the surface to 10 hPa. Bottom row (d-f): zoom into the tropopause region (40-180 hPa). The grey shaded area in panel b indicates the region of contaminated CFH data (see Section 3).

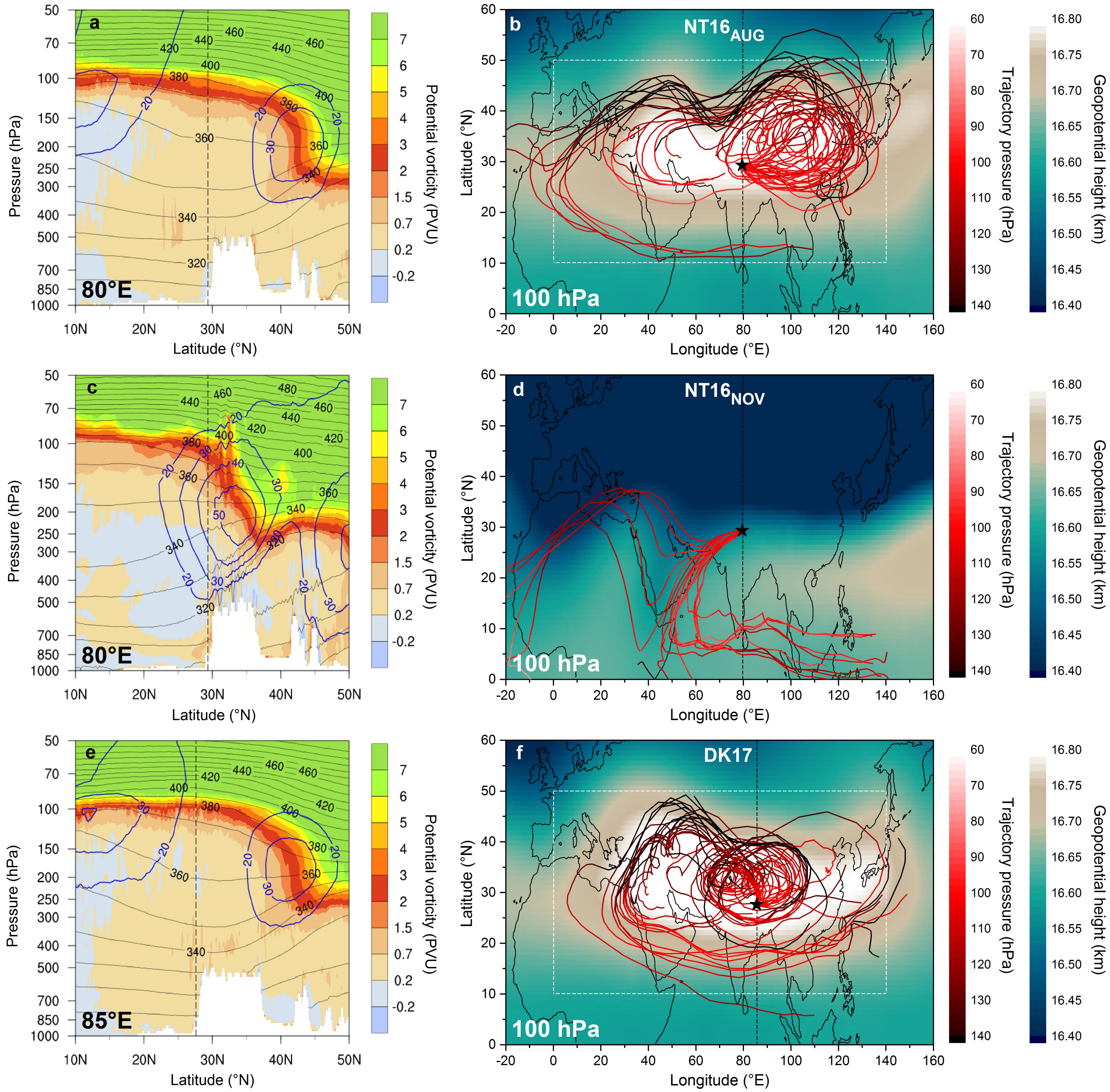

Figure 2. Left column: latitude-pressure cross-sections of potential vorticity (color scale), potential temperature (black contours, in K) and total wind speed (blue contours, in m/s) from ECMWF analysis data (horizontal resolution 0.125°, vertical resolution L137, 6-hourly) averaged over the time periods of the NT16$_{AUG}$ (panel a, longitude 80°E), NT16$_{NOV}$ (panel c, longitude 80°E) and DK17

(panel e, longitude 85°E) campaigns, as given in Table 2. Black dashed lines show the latitude of NT (a, c) and DK (e). Right column: geopotential height at 100 from ECMWF analysis data averaged over the time periods of the $NT16_{AUG}$ (b), $NT16_{NOV}$ (d) and DK17 (f) campaigns (color scale), and 2-weeks LAGRANTO backward trajectories calculated along ERA-Interim wind fields (horizontal resolution 1°, vertical resolution L60), initialized at 100 hPa at the time of each balloon sounding in $NT16_{AUG}$ (b), $NT16_{NOV}$ (d), and DK17 (f), color-coded with pressure. Black dashed lines show the longitude of NT (a, c) and DK (e). The white dashed rectangle in panels (d, f) shows the approximated ASMA area used for the confined fraction calculation (10-50°N, 0-140°E: see Section 5.2). Note that, for $NT16_{NOV}$, trajectories started 6 h before and 6 h after each sounding are also displayed (panel d).

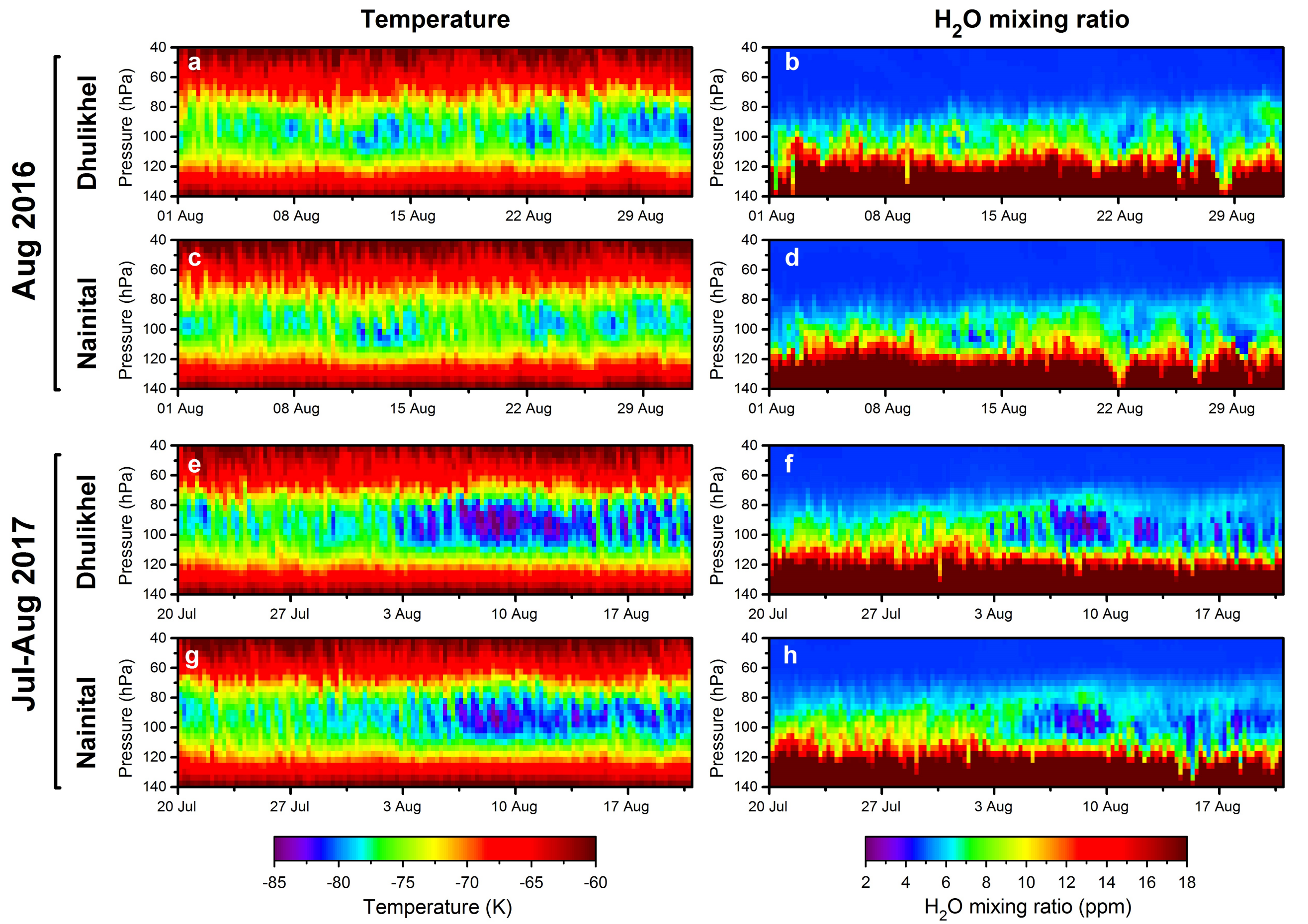

Figure 3. Time series of temperature (left column) and water vapor mixing ratio (right) as a function of pressure, from ECMWF operational analysis data (6-hourly, horizontal resolution: 0.125°, vertical resolution: L137) for the locations of NT (Panels c, d, g, h) and DK (a, b, e, f) during 1-31 August 2016 (a-d) and 20 July-21 August 2017 (e-h).

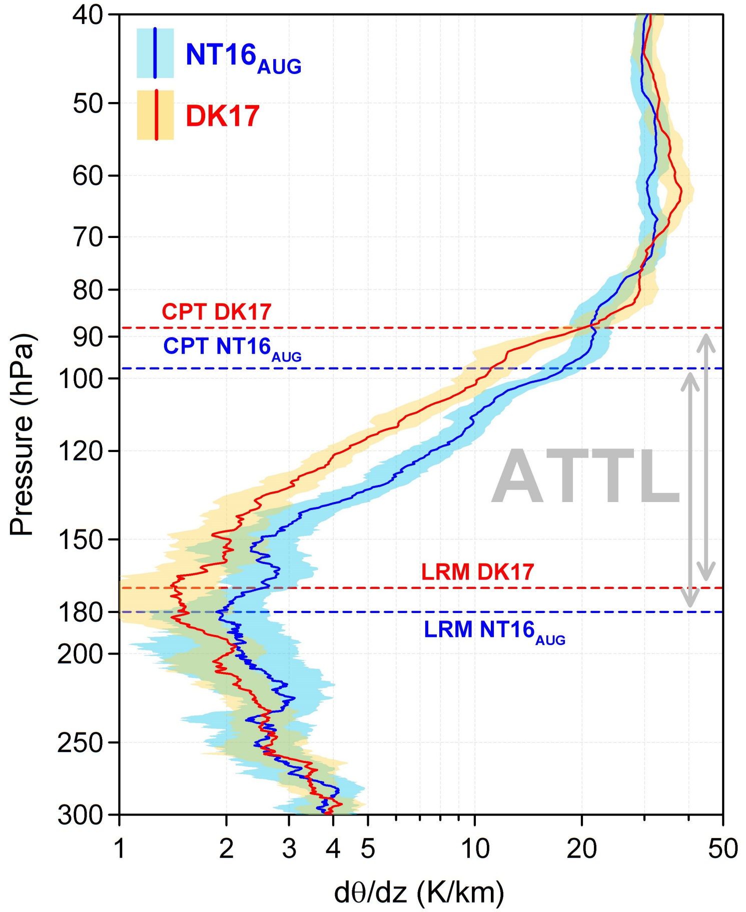

Figure 4. Mean profiles (solid lines) and standard deviations (color shading) of *dθ/dz* as a function of pressure, for NT16$_{AUG}$ (blue) and DK17 (red). Horizontal dashed lines show the mean LRM and CPT for NT16 (blue) and DK17 (red). The ATTL regions for the two datasets are highlighted by grey arrows. Note that the mean profiles and standard deviations of *dθ/dz* were smoothed with a ± 5 hPa (about 250 m) moving average to reduce the noise contributions from the geometric altitude measurement by RS41.

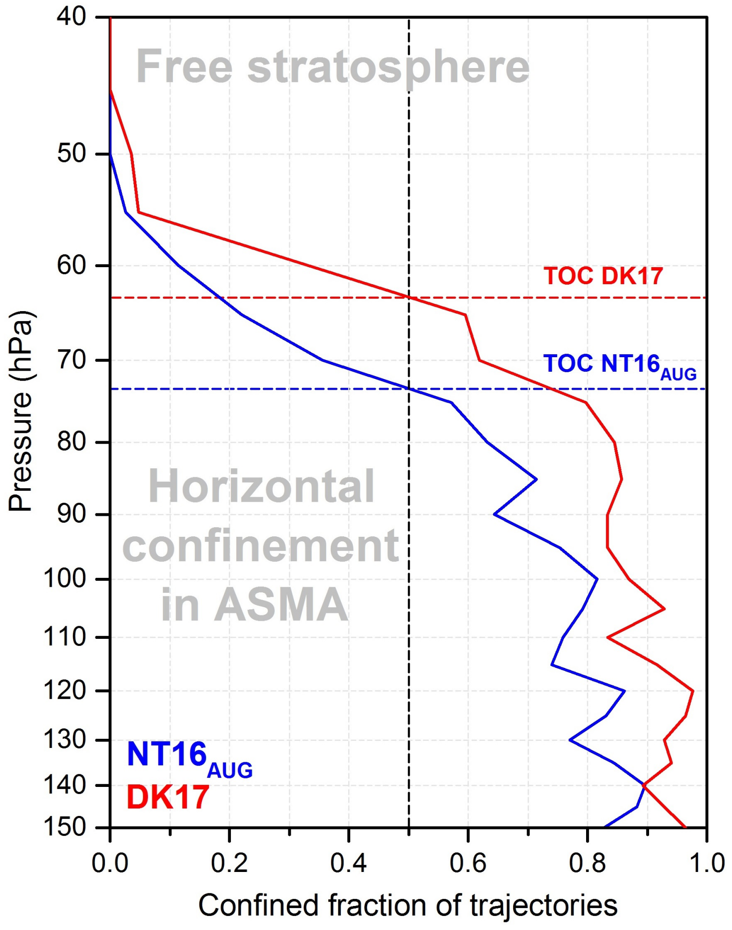

Figure 5. Confined fraction of trajectories (see Section 5.2) as a function of pressure for the $NT16_{AUG}$ (blue) and DK17 (red) campaign periods. Dashed lines mark the TOC level for NT16 (blue) and DK17 (red) and the 50% confined fraction threshold (black).

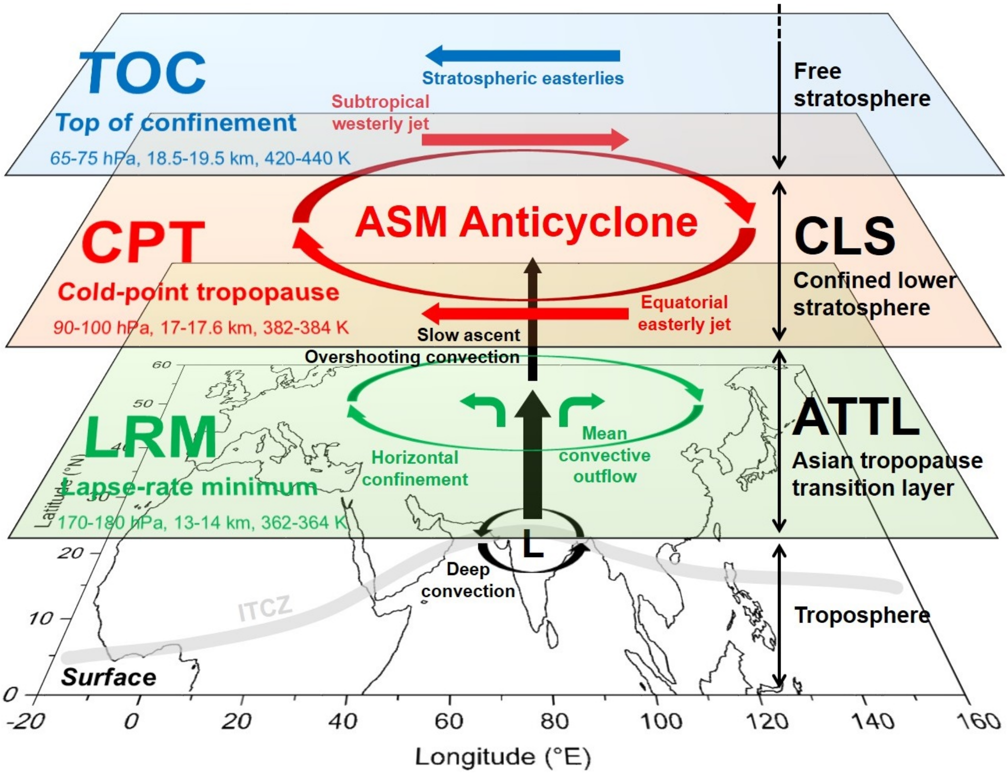

Figure 6. Schematics of the vertical structure of the UTLS above the southern slopes of the Himalayas. The Asian summer monsoon anticyclone (ASMA) consists of two layers, the Asian tropopause transition layer (ATTL) and the confined lower stratosphere (CLS). These layers are confined by three levels: the lapse rate minimum (LRM, green surface), the cold-point tropopause (CPT, red) and the top of confinement (TOC, blue). Dynamical features and relevant transport processes discussed in the paper are also sketched. Approximated pressure, altitude and potential temperature levels of the TOC, CPT and LRM derived from our $NT16_{AUG}$ and DK17 measurements are displayed on the respective surfaces.

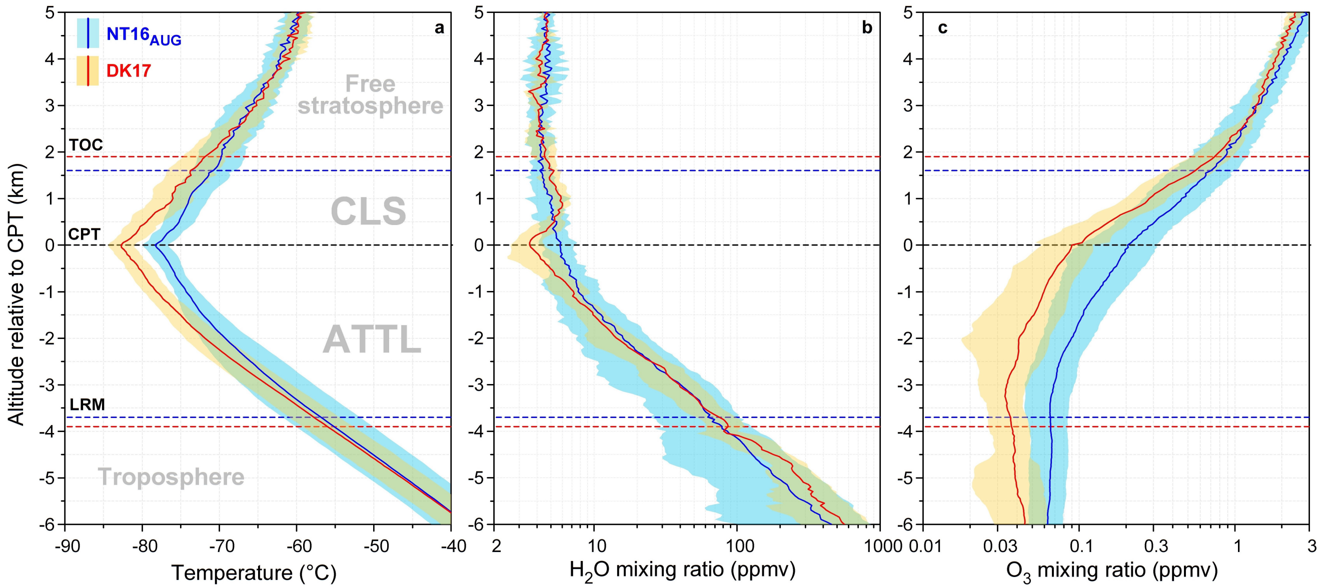

Figure 7. Mean profiles (solid lines) and standard deviations (color shading) of temperature (panel a), H_2O mixing ratio (b) and O_3 mixing ratio (c) as a function of altitude relative to CPT, for $NT16_{AUG}$ (blue) and DK17 (red). Dashed lines show the CPT (black) and the average LRM and TOC levels for NT16 (blue) and DK17 (red) (see labels in panel a). The four layers defined in Section 5.1 (troposphere, ATTL, CLS and free stratosphere) are identified by grey labels.

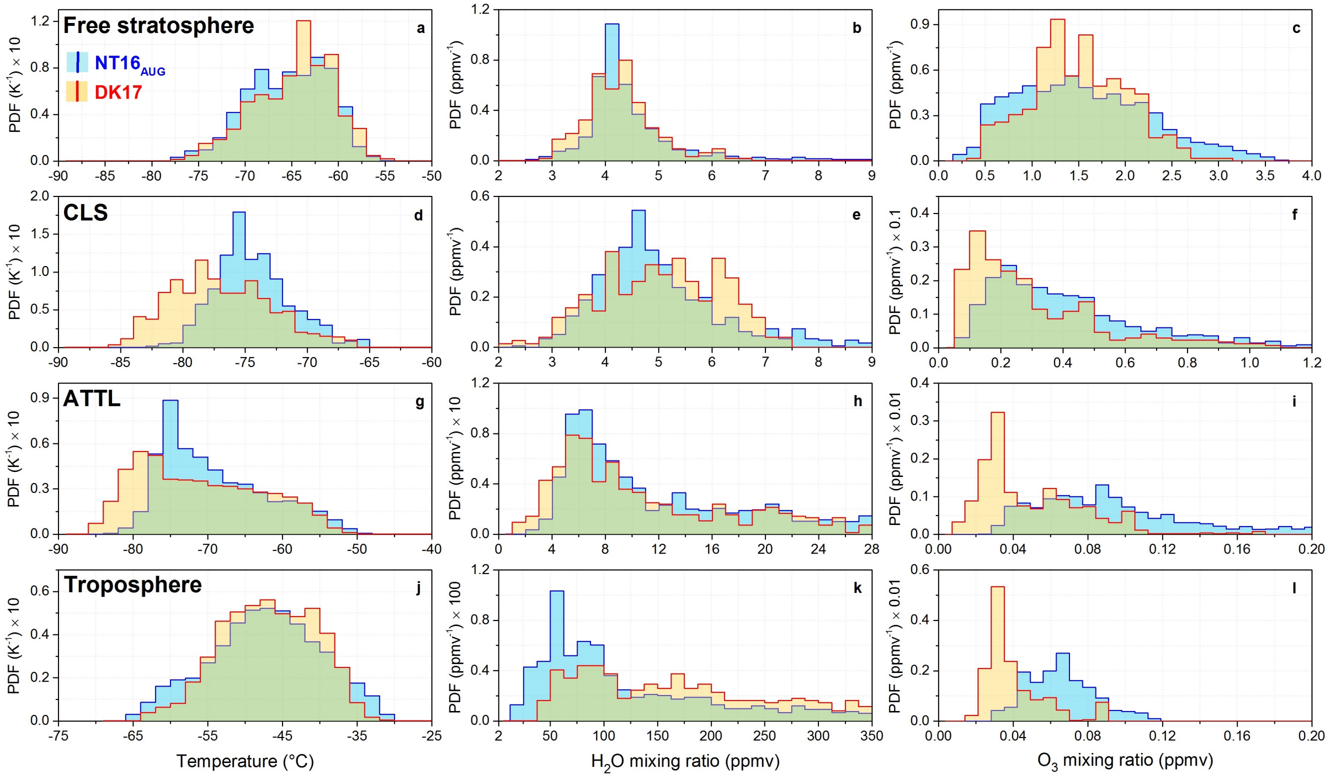

Figure 8. Probability density functions (PDFs) of temperature (left column), H_2O mixing ratio (center column) and O_3 mixing ratio (right column), calculated in the altitude regions of the free stratosphere (panels a-c), CLS (d-f), ATTL (g-h) and tropopsphere (j-l) as defined in Section 5.1, for $NT16_{AUG}$ (blue) and DK17 (red).

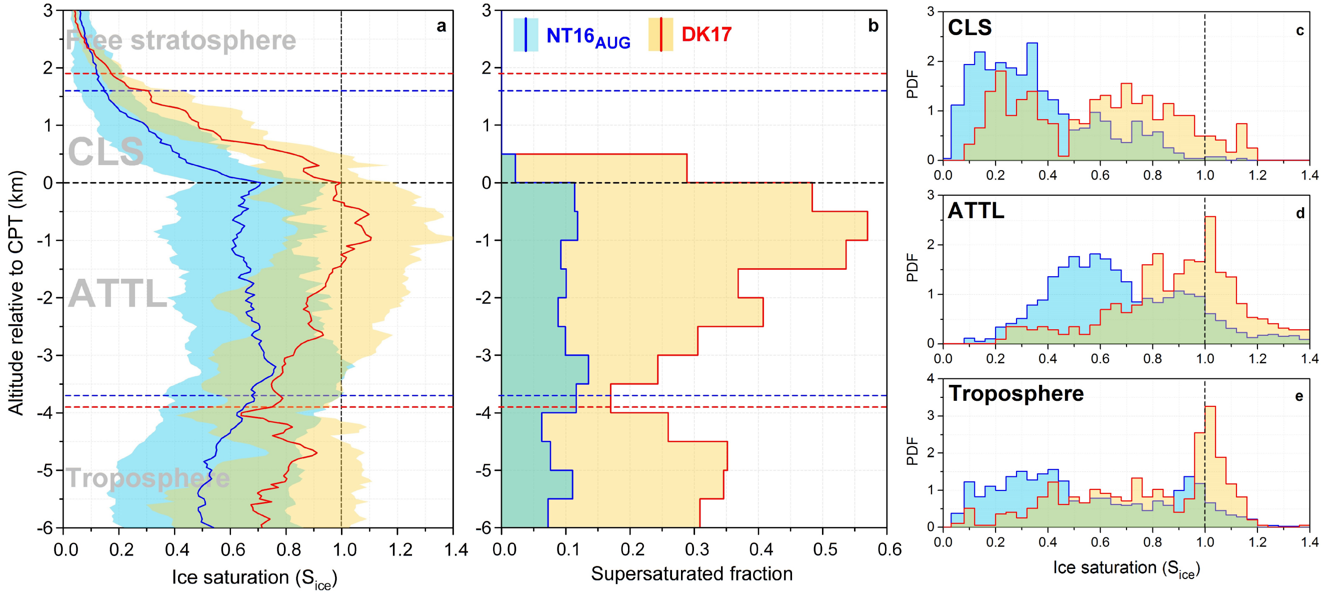

Figure 9. Panel a: mean profiles and standard deviation of ice saturation (S_{ice}) as a function of altitude relative to CPT, for NT16$_{AUG}$ (blue) and DK17 (red). Panel b: supersaturated fraction (i.e. fraction of measurements with $S_{ice} > 1$) as a function of altitude relative to CPT. Panels c, d, e: PDFs of ice saturation in the CLS, ATTL and troposphere altitude regions, respectively.

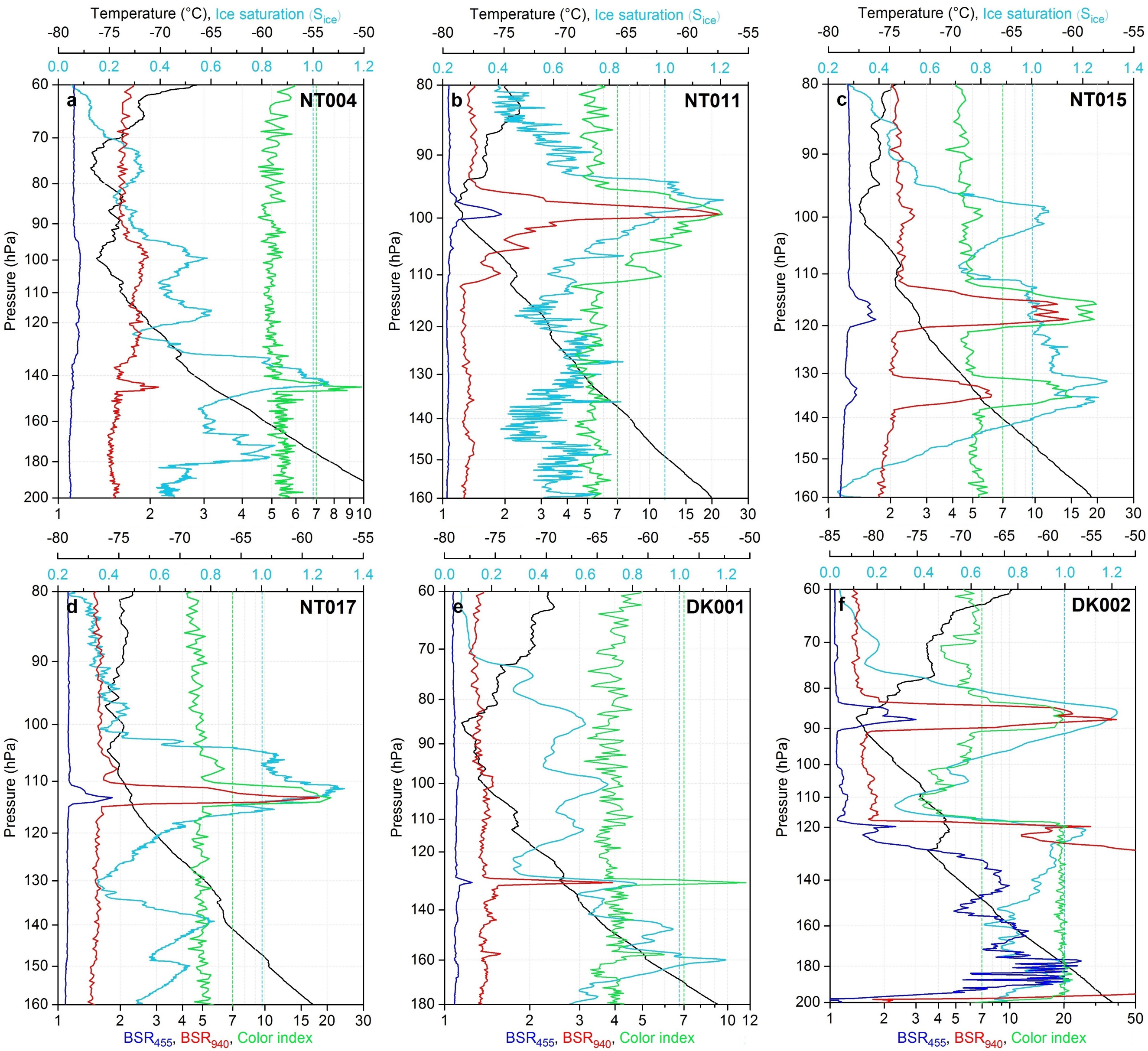

Figure 10. Examples of thin cirrus clouds measured during four individual soundings of the NT16$_{AUG}$ campaign (panels a-d) and two soundings of the DK17 campaign (e-f). Solid lines show temperature (black), ice saturation (light blue), BSR at 455 nm (*BSR_{455}*, blue), BSR at 940 nm (*BSR_{940}*, red) and Color index (green). Vertical dashed lines mark the *S_{ice}* = 1 (light blue) and Color index = 7 (green) thresholds, used for cloud-filtering (see Section 6.1). Sounding identification numbers are noted in black at the top-right corner of each panel: for date, time and payload of each sounding, see Table S1 in supplementary material.

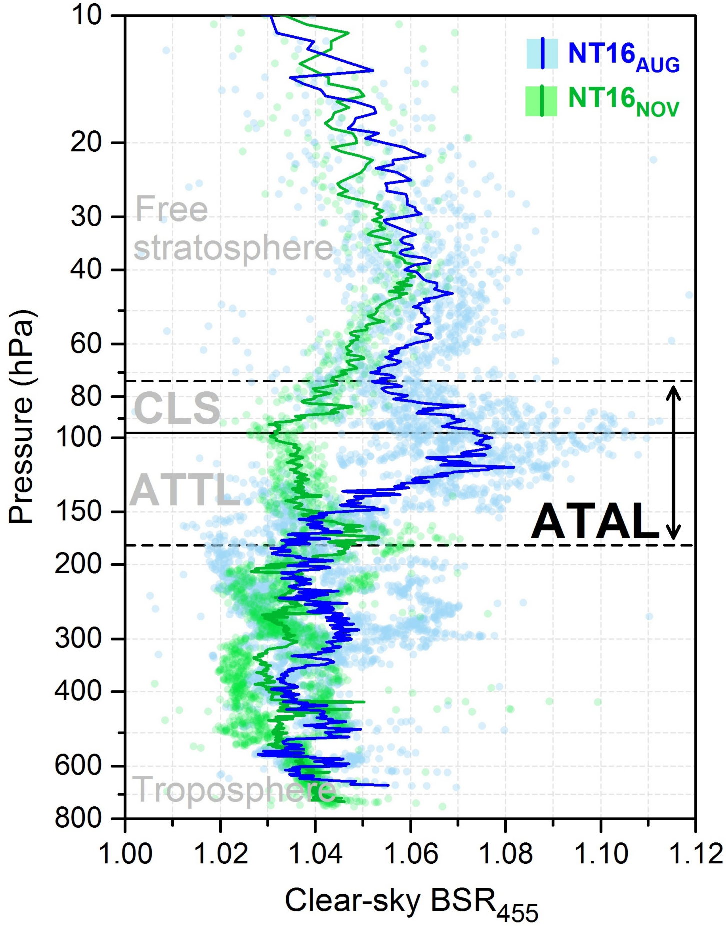

Figure 11. All clear-sky (i.e. aerosol-only) data points (dots) and mean profiles (solid lines) of BSR_{455} as a function of pressure, for $NT16_{AUG}$ (blue) and $NT16_{NOV}$ (green). Black lines show the mean LRM (dashed), CPT (solid) and TOC (dashed) levels for $NT16_{AUG}$. The troposphere, ATTL, CLS and free stratosphere regions are identified by grey labels, and the ATAL region by a black arrow.

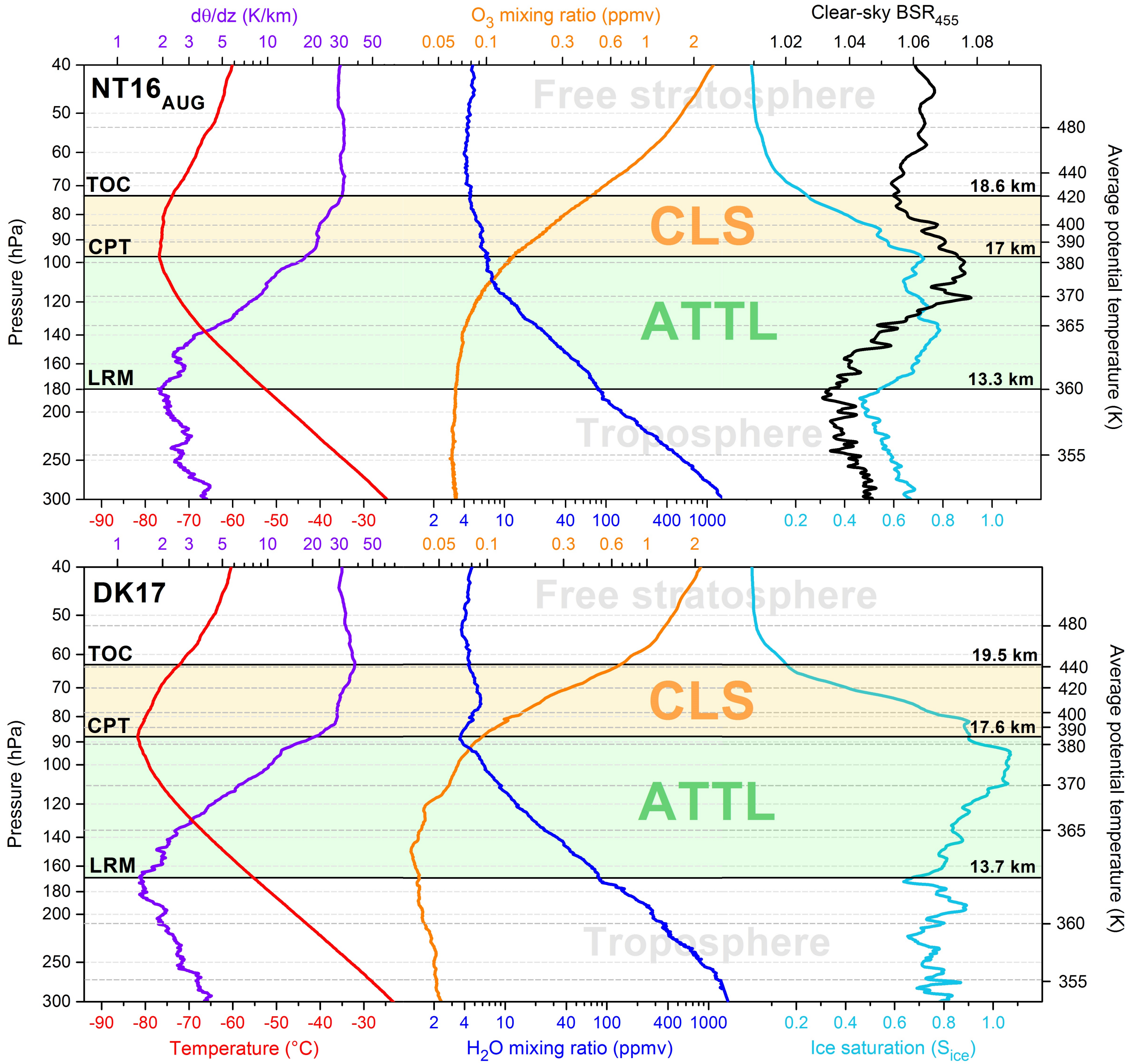

Figure 12. Mean profiles of temperature (red), *dθ/dz* (purple), H_2O mixing ratio (blue), O_3 mixing ratio (orange), ice saturation (light blue) and clear-sky aerosol BSR_{455} (black) as a function of pressure (left axis, light grey dashed lines) for $NT16_{AUG}$ (top panel) and DK17 (bottom panel). Average potential temperature leves are shown on the right axis and marked by dark grey dashed lines. Note that the pressure scale is the same for the two panels, and the potential temperature levels vary according to the measurements. The average CPT, LRM and TOC levels in the two datasets are marked by black solid lines. The ATTL and CLS layers are highlighted

by light green and orange shading, respectively. Note that the mean profiles of *$d\theta/dz$*, ice saturation and clear-sky aerosol BSR_{455} are smoothed with a ± 5 hPa (about 250 m) moving average (same as in Figure 4).